THE ASTROPHYSICAL JOURNAL, 468:269–289, 1996 September 1

STRUCTURE OF STATIONARY PHOTODISSOCIATION FRONTS

B. T. DRAINE
Princeton University Observatory, Peyton Hall, Princeton, NJ 08544; draine@astro.princeton.edu
AND
FRANK BERTOLDI
Max-Planck-Institut für Extraterrestrische Physik, D-85748 Garching, Germany; fkb@mpe-garching.mpg.de
Received 1996 January 2; accepted 1996 March 19

ABSTRACT

The structure of stationary photodissociation fronts is revisited. H_2 self-shielding is discussed, including the effects of line overlap. We find that line overlap is important for $N(H_2) \gtrsim 10^{20}$ cm^{-2}, with a factor-of-2 suppression of pumping rates at column densities $N(H_2) \approx 3 \times 10^{20}$ cm^{-2}. We compute multiline UV pumping models and compare these with simple analytic approximations for the effects of self-shielding.

The overall fluorescent efficiency of the photodissociation front is obtained for different ratios of χ/n_H (where χ characterizes the intensity of the illuminating ultraviolet radiation) and different dust extinction laws. The dust optical depth τ_{pdr} to the point where 50% of the H is molecular is found to be a simple function of a dimensionless quantity ϕ_0 depending on χ/n_H, the rate coefficient $R(T)$ for H_2 formation on grains, and the UV dust opacity. The fluorescent efficiency of the photodissocation region (PDR) also depends primarily on ϕ_0 for $\chi \lesssim 3000$ and $n_H \lesssim 10^4$ cm^{-3}; for stronger radiation fields and higher densities, radiative and collisional depopulation of vibrationally excited levels interferes with the radiative cascade. We show that the emission spectrum from the PDR is essentially independent of the color temperature T_{color} of the illuminating radiation for 10^4 K $\lesssim T_{color}$ but shows some sensitivity to the rotation-vibration distribution of newly formed H_2. The 1–0 $S(1)$/2–1 $S(1)$ and 2–1 $S(1)$/6–4 $Q(1)$ intensity ratios, the ortho/para ratio, and the rotational temperature in the $v = 1$ and $v = 2$ levels are computed as functions of the temperature and density for different values of χ/n_H.

We apply our models to the reflection nebula NGC 2023. Apparent inconsistencies between published K-band and far-red spectroscopy of this object are discussed; we adjust the two sets of observations for consistency. We are able to reproduce approximately the (adjusted) observations with models having $\chi = 5000$, $n_H = 10^5$ cm^{-3}, and a reasonable viewing angle. Further observations of NGC 2023 will be valuable to clarify the uncertain spatial structure of the emission.

Subject headings: infrared: ISM: lines and bands — ISM: reflection nebulae — molecular processes — radiative transfer — ultraviolet: ISM

1. INTRODUCTION

It is by now widely recognized that reprocessing of OB starlight in photodissociation fronts plays an important role in the overall energetics of star-forming galaxies, particularly extreme "starburst" galaxies. An important mechanism in this reprocessing is the absorption of ultraviolet photons by molecular hydrogen, followed by ultraviolet and infrared fluorescence, and, about 15% of the time, by dissociation. The vibrational fluorescence process, first noted by Gould & Harwit (1963), has been investigated by a number of authors (see, e.g., Black & Dalgarno 1976; Shull 1978; Black, Porter, & Dalgarno 1981; van Dishoeck & Black 1986; Black & van Dishoeck 1987; Sternberg 1986, 1988; Sternberg & Dalgarno 1989).

A number of theoretical investigations have advanced our understanding of photodissociation regions, or "PDRs."[1] P. M. Solomon (1965; private communication reported in Field, Somerville, & Dressler 1966) apparently was the first to propose that destruction of interstellar H_2 might be dominated by dissociating transitions to the vibrational continuum following permitted transitions to the $^1B\,\Sigma_u^+$ state; the resulting photodissociation rate was first estimated by Stecher & Williams (1967), who called attention to the potential importance of H_2 self-shielding. The H_2 self-shielding process has been studied by Shull (1978), Federman, Glassgold, & Kwan (1979), and de Jong, Dalgarno, & Boland (1980).

Tielens & Hollenbach (1985a) discussed the overall thermal and chemical structure of photodissociation fronts and applied their theoretical model to explain observed properties of the photodissociation region in Orion (Tielens & Hollenbach 1985b). Black & van Dishoeck (1987) examined in detail the fluorescent excitation of H_2 and the resulting infrared line emission. Recently, Abgrall et al. (1992) presented new data relating to the photodissociation of H_2 and carried out a more accurate treatment of the self-shielding process in order to reexamine the structure of the H/H_2 transition zone. Recent detailed self-shielding calculations for a cloud of moderate density subject to strong UV illumination (Le Bourlot et al. 1992) and for diffuse cloud conditions (Heck et al. 1992) show that in some regions line overlap significantly affected the H_2 photodissociation rate.

In a previous paper (Bertoldi & Draine 1996), we discussed the structure of coupled ionization-dissociation fronts and concluded that they were in many cases expected

[1] We use "PDR" for "photodissociation region." Note, however, that some authors use these initials for "photon-dominated region."

to be propagating at significant velocities, calling into question the interpretation of some regions, including Orion, which have been based on models of stationary photodissociation fronts. In the course of our investigation, we have reexamined the self-shielding of H_2.

In this paper, we revisit the problem of H_2 self-shielding. We confirm that line overlap can often be important, and we identify the region in parameter space where this occurs. We develop an approximate method to allow for the effects of line overlap in a statistical fashion. We apply this method to compute models for photodissociation fronts including the effects of line overlap; we also improve somewhat upon previous treatments by applying the results of recent studies of the wavelength dependence of dust extinction. We find a simple analytic description of the H_2 self-shielding function that appears to give a good approximation to the results of detailed self-shielding calculations, including line overlap.

We construct models of stationary photodissociation fronts for different densities, temperatures, and intensities of incident FUV radiation. We examine how observable properties, such as the 1–0 $S(1)$ surface brightness and the 1–0 $S(1)$/2–1 $S(1)$ and 2–1 $S(1)$/6–4 $Q(1)$ line ratios, depend on the model parameters. Two indicators of the excitation mechanism (fluorescent vs. shock) and the gas density are the ratio of the ortho- (odd J) to para-H_2 (even J) level populations and the rotational temperature within a vibrational level. We compute these quantities as a function of gas density and FUV illumination.

The famous reflection nebula NGC 2023 is a well-studied example of fluorescent emission by H_2. We attempt to reconcile published observations of this object. The available observations of NGC 2023 appear to be consistent with a photodissociation front with $n_{\rm H} \approx 10^5$ cm^{-3} irradiated by FUV radiation with intensity (relative to the Habing field) $\chi \approx 5000$.

2. COMPUTATION OF LEVEL POPULATIONS

2.1. *Equations of Statistical Equilibrium*

Let the N vibration-rotation levels of the ground electronic state of H_2 be designated by the index $l = 1, \ldots, N$. Then

$$\frac{dn_l}{dt} = Rn_{\rm H}\, n({\rm H})\delta_l + \sum_{m\neq l}\left(A_{lm} + \beta_{lm} + \sum_c n_c\, C^{(c)}_{lm}\right)n_m - n_l \sum_{m\neq l}\left(A_{ml} + \sum_c n_c\, C^{(c)}_{ml}\right) - n_l\left(\beta_{{\rm diss},l} + \sum_c n_c\, C^{(c)}_{{\rm diss},l}\right), \quad (1)$$

$$\frac{dn({\rm H})}{dt} = -2Rn_{\rm H}\, n({\rm H}) + 2\sum_m\left[\beta_{{\rm diss},m} + \sum_c n_c\, C^{(c)}_{{\rm diss},m}\right]. \quad (2)$$

The notation is as follows: R is the rate coefficient for formation of H_2 via grain catalysis; δ_l is the fraction of H_2 formed on grain surfaces that leaves the grain in level l; A_{lm} is the Einstein A-coefficient for spontaneous decay $m \rightarrow l$ ($A_{lm} = 0$ for $E_m < E_l$); β_{lm} is the effective rate for transitions $m \rightarrow l$ via ultraviolet pumping; $C^{(c)}_{lm}$ is the rate coefficient for transitions $m \rightarrow l$ due to collisions with collision partner $c \in \{{\rm H}, {\rm H}_2, {\rm He}, {\rm H}^+, e\}$; $C^{(c)}_{{\rm diss},m}$ is the rate coefficient for collisional dissociation out of level m by collisional partner c; and $\beta_{{\rm diss},m}$ is the rate of photodissociation out of level m.

The effective transition rate from level m to level l via electronically excited states u due to ultraviolet pumping is

$$\beta_{lm} = \sum_u \frac{A_{lu}}{A_{{\rm tot},u}}\,\zeta_{um}\,, \quad (3)$$

where ζ_{ul} is the rate for photoexcitation to electronically excited level u out of level l, and the total rate of spontaneous radiative decay of level u is

$$A_{{\rm tot},u} = \sum_l A_{lu} + A_{vc,u}; \quad (4)$$

here $A_{vc,u}$ is the rate of spontaneous radiative decay from level u to the vibrational continuum of the ground electronic state, resulting in dissociation. The dissociation probability for level u is

$$p_{{\rm diss},u} = A_{vc,u}/A_{{\rm tot},u}\,, \quad (5)$$

and the rate for photodissociation from level m is

$$\beta_{{\rm diss},m} = \sum_u p_{{\rm diss},u}\,\zeta_{um}\,. \quad (6)$$

The dissociation probability averaged over photoexcitations out of level $m = X(v, J)$ is

$$\langle p_{\rm diss}(v, J)\rangle = \beta_{{\rm diss},m}/\sum_u \zeta_{um}\,. \quad (7)$$

It is convenient to define the diagonal elements A_{ll}, C_{ll}, and β_{ll} to be

$$A_{ll} \equiv -\sum_{m\neq l} A_{ml}\,, \quad (8)$$

$$\beta_{ll} \equiv -\sum_{m\neq l}\beta_{ml} - \beta_{{\rm diss},l}\,, \quad (9)$$

$$C^{(c)}_{ll} \equiv -\sum_{m\neq l} C^{(c)}_{ml} - C^{(c)}_{{\rm diss},m}\,. \quad (10)$$

Equation (1) then becomes

$$\frac{dn_l}{dt} = Rn_{\rm H}\, n({\rm H})\delta_l + \sum_m D_{lm}\, n_m\,, \quad (11)$$

$$\frac{dn({\rm H})}{dt} = -2Rn_{\rm H}\, n({\rm H}) + 2\sum_m D_{{\rm diss},m}\, n_m\,, \quad (12)$$

where

$$D_{lm} \equiv A_{lm} + \beta_{lm} + \sum_c n_c\, C^{(c)}_{lm}\,, \quad (13)$$

$$D_{{\rm diss},m} \equiv \beta_{{\rm diss},m} + \sum_c n_c\, C^{(c)}_{{\rm diss},m}\,. \quad (14)$$

We include the 299 bound states of H_2 with $J \leq 29$ in our calculations.

2.2. *Radiative Rates*

We designate the vibration-rotation levels of the ground electronic state $X\,^1\Sigma_g^+$ by $X(v, J)$, and the first three electronically excited states $B\,^1\Sigma_u^+$, $C\,^1\Pi_u^+$, and $C\,^1\Pi_u^-$ by $B(v, J)$, $C^+(v, J)$, and $C^-(v, J)$.

Energy levels E_u, transition probabilities A_{lu}, and dissociation probabilities $p_{{\rm diss},u}$ have been published by Abgrall & Roueff (1989) and Abgrall et al. (1992, 1993a, 1993b).

We used data generously provided by Roueff (1992), covering levels up to $J = 29$. As discussed by Abgrall et al. (1992), these new data include dissociation probabilities $p_{{\rm diss},u}$ for the $C^+(v, J)$ levels that are considerably larger than the dissociation probabilities of Stephens & Dalgarno (1972), which were used for both $C^+(v, J)$ and $C^-(v, J)$ in

earlier detailed modeling (see, e.g., van Dishoeck & Black 1986; Black & van Dishoeck 1987). As a result, we find somewhat larger overall dissociation probabilities.

The transition probabilities A_{lu} and dissociation probabilities $p_{\mathrm{diss},u}$ are assumed to be independent of the energy of the photon responsible for photoexcitation to level u: the branching ratios for radiative decay out of level u are assumed to *not* depend on whether the photoexcitation to level u was due to a photon that was precisely resonant ($\lambda = \lambda_{lu}$) or far out on the damping wings of the transition (e.g., $\lambda = 1.001\lambda_{lu}$). While this approximation is usual, it should be remembered that it is probably not exact.

2.3. *Collisional Rates*

We include inelastic collisions with H, He, H_2, H^+, and e^-, with collisional rate coefficients as described in Draine & Bertoldi (1996). For H–H_2 collisions, inelastic cross sections have been computed by Mandy & Martin (1993, 1996) using semiclassical trajectory calculations; Martin & Mandy (1995) have provided fits to the resulting rate coefficients for $450 < T < 20{,}000$ K. In the present application, it is necessary to extrapolate to temperatures $T < 450$ K. The Martin & Mandy fitting function is

$$\log_{10}\langle\sigma v\rangle = a + bz + cz^2 - d\left(\frac{4500\ \mathrm{K}}{T} - 1\right), \quad (15)$$

where $z \equiv \log_{10}(T/4500\ \mathrm{K})$. Even for downward transitions, the coefficient d is typically large enough that this function declines very rapidly with decreasing temperature at low temperatures. Furthermore, comparison of semiclassical trajectory calculations and quantal calculations indicate that the former approximation substantially underestimates the inelastic cross sections near the energy threshold (Lepp, Buch, & Dalgarno 1995). Accordingly, we use equation (15) for $T > \theta = 600$ K, but for $T < \theta$ we take, for downward transitions,

$$\log_{10}\langle\sigma v\rangle = a + bz + cz^2 - d\left(\frac{9000\ \mathrm{K}}{\theta} - 1 - \frac{4500\ \mathrm{K}\,T}{\theta^2}\right); \quad (16)$$

upward transitions are obtained from detailed balance. This expression joins smoothly to equation (15) at $T = \theta$ but declines less dramatically for $T < \theta$.[2] Since we have extrapolated in a rather arbitrary manner, it is clear that quantal calculations with an accurate potential surface are needed to provide better estimates of the low-temperature H–H_2 rate coefficients.

H^+ is treated as a species with a fixed abundance $x_{\mathrm{H}} \equiv n(H^+)/n_{\mathrm{H}} = 1 \times 10^{-4}$; we assume[3] $n_e/n_{\mathrm{H}} = 3 \times 10^{-4}$.

2.4. H_2 *Formation on Grains*

As discussed elsewhere (Draine & Bertoldi 1996), we assume that H atoms recombine on grain surfaces to form H_2 at a rate per volume

$$\left[\frac{dn(\mathrm{H_2})}{dt}\right]_{\mathrm{form}} = Rn_{\mathrm{H}}\,n(\mathrm{H}), \quad (17)$$

with

$$R = 6 \times 10^{-18} T^{1/2}\ \mathrm{cm^3\ s^{-1}}; \quad (18)$$

this adopted value of R is $\frac{2}{3}$ of the value adopted by Black & van Dishoeck (1987) for most of their model calculations. For $T = 70$ K, this rate is ~ 1.7 times larger than the value of R inferred by Jura (1975) from *Copernicus* observations of H_2 in diffuse clouds.

The rovibrational distribution $\delta(v, J)$ of the newly formed H_2 is taken to be of the form (Draine & Bertoldi 1996)

$$\delta(v, J) = \delta(0, 0) g_n(J)(1 + v)\exp\left[-E(v, J)/kT_f\right], \quad (19)$$

where $g_n = 1, 3$ for even, odd J. We note that this distribution (19) does *not* include a rotational degeneracy factor $(2J + 1)$ and *does* include a factor $(1 + v)$; these deviations from a thermal distribution function are intended to enhance the populations of high-v states relative to high-J states. In the present paper, we take $T_f = 5 \times 10^4$ K, in which case the newly formed H_2 has an ortho/para ratio = 2.78, $\langle v\rangle = 5.3$, $\langle J\rangle = 8.7$, $\langle J^2\rangle^{1/2} = 10.7$, and a mean vibration-rotation energy of 2.89 eV.

3. RADIATION FIELD

The efficacy of H_2 self-shielding depends upon the distribution of H_2 over the different levels $X(v, J)$, which in turn depends upon the density and temperature of the gas and the incident radiation field.

In neutral regions, pumping of H_2 is primarily effected by far-ultraviolet photons in the 1110–912 Å range.[4] Habing (1968) estimated the intensity of interstellar starlight at $\lambda = 1000$ Å to be $\lambda u_\lambda = 4 \times 10^{-14}$ ergs cm^{-3}. We will consider various radiation fields u_λ, and will characterize the intensity of each at 1000 Å, relative to Habing's estimate, by the dimensionless factor

$$\chi \equiv \frac{(\lambda u_\lambda)_{1000\ \text{Å}}}{4 \times 10^{-14}\ \mathrm{ergs\ cm^{-3}}}. \quad (20)$$

In Table 1 we list spectral forms that have been considered by various workers. For each spectrum we list the photon flux in the 1110–912 Å interval,

$$F \equiv \int_{912\ \text{Å}}^{1110\ \text{Å}} h^{-1}\lambda u_\lambda\, d\lambda, \quad (21)$$

the logarithmic derivative $d\ln u_\nu/d\ln\nu$ evaluated at 1000 Å, and the color temperature T_{color}, the temperature of a blackbody having the same logarithmic derivative at 1000 Å.

Habing (1968) estimated the average radiation field at 1000, 1400, and 2200 Å. We note that Habing's values can be fitted by

$$\lambda u_\lambda = \left(-\frac{25}{6}\lambda_3^3 + \frac{25}{2}\lambda_3^2 - \frac{13}{3}\lambda_3\right) \times 10^{-14}\ \mathrm{ergs\ cm^{-3}}, \quad (22)$$

[2] Even so, the resulting rate coefficients for $(0, 2) \rightarrow (0, 1)$ and $(0, 3) \rightarrow (0, 0)$ at $T = 200$ K are only 2.9×10^{-14} cm^3 s^{-1} and 1.4×10^{-14} cm^3 s^{-1}, smaller than the best estimates of Lepp et al. by factors of 30 and 200, respectively.

[3] For a photoionized metal abundance $n(M^+)/n_{\mathrm{H}} = 2 \times 10^{-4}$ (primarily C^+), a hydrogen ionization rate $\zeta_{\mathrm{H}} = 8 \times 10^{-18}(T/10^2\ \mathrm{K})^{-0.64}(n_{\mathrm{H}}/40\ \mathrm{cm^{-3}})\ \mathrm{s^{-1}}$ (due to either cosmic rays or X-rays) would sustain a hydrogen ionization fraction $x_{\mathrm{H}} = 1 \times 10^{-4}$.

[4] Photons shortward of 912 Å are of course absorbed by atomic hydrogen. H_2 in the $v = 0$ levels has only weak absorptions longward of 1110 Å: the longest wavelength absorption out of the $J = 0$ and 1 levels is the Lyman 0–0 $P(1)$ line at 1110.066 Å, with an oscillator strength $f_{lu} = 0.00058$ [as compared to the much stronger 7–0 $R(1)$ (i.e., $v_u = 7$, $v_l = 0$, J_u–$J_l = 1$, $J_l = 1$) line at 1013.434 Å, with $f_{lu} = 0.020$]. While there are weak absorptions out of $v = 0$, $J = 2, 3, 4, 5, \ldots$ longward of 1110 Å [Lyman 0–0 $P(2)$, $P(3)$, $P(4)$, $P(5)$, ... at 1112.5, 1115.9, 1120.3, 1125.5 Å ..., with $f_{lu} = 0.00070, 0.00074, 0.00076, 0.00076$ ...], it is fair to assume that the bulk of UV pumping of H_2 is due to photons in the 1110–912 Å interval.

TABLE 1

INTERSTELLAR ULTRAVIOLET RADIATION FIELDS ($\lambda > 912$ Å)

Radiation Field	χ	F/χ (cm^{-2} s^{-1})	$d\ln u_\nu/d\ln\nu$ (at 1000 Å)	T_{color} (10^4 K)
$u_\nu = 2.84\times10^{-18}(4\pi/c)B_\nu(4\times10^4\ \mathrm{K})$.....	1	1.186×10^7	−0.302	4.00
$u_\nu \propto \nu^{-1}$		1.195×10^7	−1	3.67
$u_\nu = 3.04\times10^{-19}(4\pi/c)B_\nu(3\times10^4\ \mathrm{K})$.....	1	1.197×10^7	−1.836	3.00
$u_\nu \propto \nu^{-2}$ (eq. [24])		1.208×10^7	−2	2.90
Habing 1968 (eq. [22])	1	1.222×10^7	−3.043	2.39
$u_\nu = 1.06\times10^{-16}(4\pi/c)B_\nu(2\times10^4\ \mathrm{K})$.....	1	1.237×10^7	−4.199	2.00
Mathis, Mezger, & Panagia 1983	1.23	1.232×10^7	−5.417	1.71
Black & van Dishoeck 1987	$2.23I_{UV}$	1.218×10^7	−6	1.60
Draine 1978 (eq. [23])	1.71	1.232×10^7	−8.119	1.29
$u_\nu = 1.42\times10^{-13}(4\pi/c)B_\nu(10^4\ \mathrm{K})$	1	1.510×10^7	−11.39	1.00

where $\lambda_3 \equiv \lambda/10^3$ Å; this is the spectrum listed as "Habing" in Table 1.

Draine (1978) approximated UV starlight by the relatively soft radiation field

$$\lambda u_\lambda = 4\times10^{-14}\chi\lambda_3^{-5}(31.016\lambda_3^2 - 49.913\lambda_3 + 19.897)\ \mathrm{ergs\ cm^{-3}}, \quad (23)$$

with $\chi = 1.71$.

Roberge, Dalgarno, & Flannery (1981) used a radiation field similar to equation (23). This radiation field was employed by van Dishoeck & Black (1986) in their modeling of diffuse clouds and by Black & van Dishoeck (1987) in their models of photodissociation fronts. As seen in Table 1, this spectrum is somewhat harder than equation (23).

As an example of the radiation field expected in a photodissociation front near an OB star, we consider the power-law spectrum $u_\nu \propto \nu^{-2}$:

$$\nu u_\nu(x=0) \equiv \lambda u_\lambda(x=0) = 4\times10^{-14}\chi\lambda_3\ \mathrm{ergs\ cm^{-3}}. \quad (24)$$

This spectrum has $T_{color} = 29{,}000$ K, corresponding to the spectrum of a B0 star. We use this spectrum in most of the model calculations; as we show below (§ 6.2 and Fig. 14), the properties of the PDR are insensitive to the spectrum for color temperatures $T_{color} \gtrsim 10^4$ K, so that the models presented here have general applicability to PDRs illuminated by stars of spectral type A0 and earlier.[5]

Pumping rates and dissociation rates for optically thin H_2 in various rotation-vibration states are given in Table 2 for the radiation fields (24) and (23). Also given in Table 1 is the probability $p_{diss}(v, J)$ that photoexcitation out of level $X(v, J)$ will be followed by dissociation and the probability $\langle p_{ret}(v, J)\rangle$ that photoexcitation out of $X(v, J)$ will be followed by direct spontaneous decay back to the original level $X(v, J)$. Since there are many possible UV transitions possible out of any given level $X(v, J)$, both p_{diss} and $\langle p_{ret}\rangle$ depend on the shape of the illuminating spectrum, but Table 2 shows that for unshielded H_2, the changes in $\langle p_{diss}\rangle$ or p_{ret} are typically only a few percent when the shape of the radiation field is changed. Note, however, that changes in the radiation field due to self-shielding can lead to larger

[5] Late B-type stars of course do not have large luminosities in the 1110–912 Å interval and can only produce large χ values close to the star.

TABLE 2

PUMPING AND DISSOCIATION RATES FOR UNSHIELDED H_2

H_2 Level (v, J)	u_λ FROM EQ. (24), $\chi = 1$			u_λ FROM EQ. (23), $\chi = 1$		
	ζ_{pump} (s^{-1})	$\langle p_{diss}\rangle$	$\langle p_{ret}\rangle$	ζ_{pump} (s^{-1})	$\langle p_{diss}\rangle$	$\langle p_{ret}\rangle$
(0, 0).....	3.08(−10)	0.134	0.077	2.77(−10)	0.117	0.071
(0, 1).....	3.09(−10)	0.136	0.101	2.79(−10)	0.119	0.097
(0, 2).....	3.13(−10)	0.135	0.096	2.84(−10)	0.119	0.091
(0, 3).....	3.15(−10)	0.145	0.094	2.91(−10)	0.129	0.089
(0, 4).....	3.21(−10)	0.154	0.096	3.00(−10)	0.139	0.092
(0, 5).....	3.26(−10)	0.155	0.098	3.11(−10)	0.141	0.093
(0, 6).....	3.38(−10)	0.169	0.098	3.27(−10)	0.157	0.094
(0, 7).....	3.47(−10)	0.170	0.098	3.44(−10)	0.160	0.096
(0, 8).....	3.57(−10)	0.185	0.096	3.63(−10)	0.175	0.093
(0, 9).....	3.71(−10)	0.202	0.096	3.86(−10)	0.195	0.094
(1, 0).....	3.52(−10)	0.083	0.080	4.19(−10)	0.051	0.083
(1, 1).....	3.60(−10)	0.090	0.109	4.23(−10)	0.055	0.114
(1, 2).....	3.64(−10)	0.091	0.101	4.29(−10)	0.056	0.106
(1, 3).....	3.68(−10)	0.091	0.100	4.36(−10)	0.057	0.104
(1, 4).....	3.73(−10)	0.096	0.100	4.46(−10)	0.062	0.104
(1, 5).....	3.81(−10)	0.108	0.098	4.58(−10)	0.075	0.102
(2, 0).....	4.23(−10)	0.111	0.081	5.67(−10)	0.078	0.084
(2, 1).....	4.25(−10)	0.106	0.110	5.70(−10)	0.074	0.116
(2, 2).....	4.30(−10)	0.109	0.101	5.76(−10)	0.076	0.107
(2, 3).....	4.35(−10)	0.117	0.099	5.84(−10)	0.083	0.104
(2, 4).....	4.39(−10)	0.115	0.097	5.94(−10)	0.084	0.102
(2, 5).....	4.44(−10)	0.126	0.101	6.06(−10)	0.095	0.106
$T_r = 50$	3.08(−10)	0.134	...	2.77(−10)	0.117	...
$T_r = 100$.....	3.09(−10)	0.135	...	2.78(−10)	0.119	...
$T_r = 200$.....	3.09(−10)	0.136	...	2.79(−10)	0.119	...

changes in, for example, $\langle p_{\rm diss}\rangle$, as the relative importance of inherently weak absorption transitions increases. Indeed, for complete photodissociation fronts we find (see § 5.2) that $\langle p_{\rm diss}\rangle \approx 0.15$ averaged over all UV absorptions.

Shull (1978) has noted that when the UV intensity is high, photoexcitation out of vibrationally excited levels can affect the "infrared cascade" following UV pumping. For example, with no shielding, the rate of photoexcitation out of the $X(1, 3)$ level is $3.30 \times 10^{-10}\chi$ s^{-1} for the spectrum (24). Since the total rate for spontaneous decay out of $X(1, 3)$ is 8.35×10^{-7} s^{-1}, we see that in the optically thin part of the photodissociation front [$N(\rm H_2) \lesssim 10^{14}$ cm^{-2}] UV pumping will significantly interfere with the "infrared cascade" for $\chi \gtrsim 2500$. Our calculations explicitly include UV pumping out of all levels $X(v, J)$.

4. SHIELDING OF $\rm H_2$

4.1. *Shielding by Dust*

The wavelength dependence of interstellar extinction has been discussed by Cardelli, Clayton, & Mathis (1989, hereafter CCM) and O'Donnell (1994) and has been found to be very nearly a one-parameter family, where the parameter may be taken to be $R_V \equiv A_V/E(B-V)$. The extinction at $\lambda > 9000$ Å appears to be "universal," with an extinction cross section per H nucleus $\sigma_{\rm ext}(9000\ \text{Å}) = 2.4 \times 10^{-22}$ cm^2. The "average" extinction curve has $N_{\rm H}/E(B-V) = 5.8 \times 10^{21}$ cm^{-2} (Bohlin, Savage, & Drake 1978) and $R_V \equiv A_V/E(B-V) = 3.1$; the CCM extinction curve then predicts an extinction cross section per H of $\sigma_{\rm ext}(1000\ \text{Å}) = 2.62 \times 10^{-21}$ cm^2. In dense molecular regions, however, the extinction appears to typically have larger values of $R_V = 4$–6 (Mathis 1990), with a less steep rise in the ultraviolet. We will consider two cases: $R_V = 3.1$ (for diffuse clouds) and $R_V = 5.5$ (the value observed toward θ^1 Ori C in the Trapezium, possibly representative of very dense clouds); for $R_V = 5.5$, CCM predict $\sigma_{\rm ext}(1000\ \text{Å}) = 8.16 \times 10^{-22}$ cm^2.

We consider plane-parallel clouds, with the radiation incident normally on *one* cloud surface. We do not attempt to treat scattering in any detail but simply assume that the effect of dust is to attenuate the incident radiation field by a factor $\exp(-\tau_{d,\lambda})$, where $\tau_{d,\lambda} = N_{\rm H}\sigma_{d,\lambda}$, $N_{\rm H} = N(\rm H) + 2N(\rm H_2) + N(\rm H^+)$ is the total hydrogen column density between the point of interest and the cloud surface, and $\sigma_{d,\lambda}$ is the effective attenuation cross section at wavelength λ.

The dust albedo in the 1110–912 Å region is uncertain; a recent study of the reflection nebula NGC 7023 near $\lambda = 1000$ Å finds an albedo $\sim$0.4 and a scattering asymmetry factor $\langle\cos\theta\rangle \approx 0.75$ (Witt et al. 1993). The effects of scattering are of course complicated and geometry dependent, but if the albedo is 0.4, then $0.6 < \sigma_d/\sigma_{\rm ext} < 1$. At $\lambda = 1000$ Å, we take the effective attenuation cross section to be $\sigma_{d,1000} = 2 \times 10^{-21}$ cm^2 for $R_V = 3.1$ and 6×10^{-22} cm^2 for $R_V = 5.5$—about 75% of the estimated extinction cross sections at this wavelength. At wavelengths other than 1000 Å, we take the attenuation cross section $\sigma_{d,\lambda} = (A_\lambda/A_{1000})\sigma_{d,1000}$, where the ratio of extinction cross sections A_λ/A_{1000} is given by the CCM extinction curve for $R_V = 3.1$ or $R_V = 5.5$.

4.2. *Self-Shielding Neglecting Line Overlap*

Each level $X(v, J)$ has many allowed transitions to vibration-rotation levels of the B, C^+, and C^- electronic states. Let subscripts l and u denote the lower and upper levels. Let a continuum radiation field be incident on the cloud, with specific energy density u_λ at the cloud surface. Neglecting line overlap, the rate of photoexcitation $l \rightarrow u$ for an $\rm H_2$ molecule in level l is simply

$$\zeta_{ul}(N_l) = \frac{\lambda_{ul}^2 u_\lambda}{h}\left(\frac{dW_{ul}}{dN_l}\right)\exp\left[-\tau_d(v_{ul})\right], \tag{25}$$

where N_l is the column density of $\rm H_2$ in level l, $\tau_d(v)$ is the "attenuation" optical depth due to dust, and $W_{ul}(N_l)$ is the dimensionless equivalent width for the transition $l \rightarrow u$:

$$W_{ul}(N_l) = \int \frac{d\lambda}{\lambda}\left[1 - \exp\left(-N_l\sigma_{ul}\right)\right], \tag{26}$$

where the photoabsorption cross section $\sigma_{ul}(\lambda)$, given by the Voigt line profile function, depends upon the oscillator strength f_{lu} for the transition, the usual Doppler broadening parameter $b = \text{FWHM}/(4\ln 2)^{1/2}$, and the intrinsic broadening $A_{{\rm tot},u}$ of the upper level. We use accurate numerical approximations for dW_{ul}/dN_l and $W_{ul}(N_l)$ given by Rodgers & Williams (1974).

4.3. *Self-Shielding Including Line Overlap*

For small column densities, equation (25) will give a good estimate of the effects of self-shielding. At large column densities, however, lines may be shielded in part by overlap with other lines, as noted by Black & Dalgarno (1977). Many previous treatments have neglected this overlap: Black & van Dishoeck (1987) cited Roberge (1981) and Sternberg (1986) as having shown line overlap to be negligible for normal dust-to-gas ratios. More recently, detailed transfer calculations (Abgrall et al. 1992; Le Bourlot et al. 1992) have found that line overlap can become important under some conditions. Here we reconsider the importance of line overlap.

Exact treatment of the effects of line overlap requires explicit calculation of the full radiation field as a function of frequency at each point. However, a simple estimate for the effects of line overlap may be obtained by first noting that the strong $\rm H_2$ absorption lines originate from the $v = 0$ level and will therefore be almost entirely confined to the wavelength range 1110–912 Å (see footnote 4). Therefore, for lines with $\lambda_{ul} > 1110$ Å we will neglect line overlap and will use equation (25).

We note that the wavelength range 1110–912 Å includes H Lyβ, γ, δ, ... at 1025.72, 972.54, 949.75, ... Å. Since the PDR may develop large column densities N(H), these lines may suppress the pumping rates for nearby $\rm H_2$ lines.

For the lines with $912 < \lambda_{ul} < 1110$ Å, we note that the total equivalent width of the ensemble of lines, including H lines and the effects of line overlap, will asymptotically approach $W_{\rm max} \approx \ln(1110/912) \approx 0.2$ at large column densities. If we now treat the lines "democratically"—equally subject to the effects of line overlap—then we may approximate the effects of line overlap by considering a modified equivalent width $\tilde{W}_{ul}$ defined by

$$\frac{d\tilde{W}_{ul}}{dN_l} = \frac{dW_{ul}}{dN_l}\exp\left(\frac{-W}{W_{\rm max}}\right) \quad \text{for} \quad 912 < \lambda_{ul} < 1110\ \text{Å}, \tag{27}$$

where

$$W \equiv \sum_l {\sum_u}' W_{ul} + \sum_{n=3}^{15} W(\mathrm{H1}\text{–}n) \quad \text{for } 912 < \lambda_{ul} < 1110 \text{ Å} ; \tag{28}$$

the prime indicates that we restrict the sum to transitions with $1110 < \lambda_{ul} < 912$ Å. For $n \gtrsim 10$ the H Lyman damping wings are not important, and the Lyman series lines blend together to form a continuum for $n \gtrsim 39(3 \text{ km s}^{-1}/b)^{1/3}$, or $\lambda \lesssim [911.76 + 0.60(b/3 \text{ km s}^{-1})^{2/3}]$ Å. We will somewhat arbitrarily consider the H Lyman lines individually up to $n = 15$; the H1–15 line is at 915.83 Å. The damping constants $A_{\rm tot}$ for the np levels were obtained by summing over A coefficients for the different decay channels; the latter were computed using radial integrals tabulated by Green, Rush, & Chandler (1957). We will see below that absorption by the H Lyman lines has only a small effect on the H_2 pumping rates.

It is easily seen that

$$\tilde{W} \equiv \sum_u {\sum_l}' \tilde{W}_{ul} + \sum_{n=3}^{15} \tilde{W}(\mathrm{H1}\text{–}n) = W_{\rm max}[1 - \exp(-W/W_{\rm max})] , \tag{29}$$

so that $\tilde{W} \to W_{\rm max}$ as $W \to \infty$. To allow for line overlap, therefore, we take the pumping rates to be

$$\zeta_{ul}(N_l) = \frac{\lambda_{ul}^2 u_\lambda}{h} \left(\frac{dW_{ul}}{dN_l}\right) \exp\left(\frac{-W}{W_{\rm max}}\right) \exp[-\tau_d(\lambda_{ul})] , \tag{30}$$

with W_{ul} given by equation (26), W given by equation (28), and $W_{\rm max} = 0.2$.

The pumping rate and photodissociation rate out of level l are simply

$$\zeta_{{\rm pump},l} = \sum_u \zeta_{ul} , \tag{31}$$

$$\zeta_{{\rm diss},l} = \sum_u \zeta_{ul} p_{{\rm diss},u} . \tag{32}$$

The effective pumping rate and photodissociation rate per H_2 molecule are just

$$\zeta_{\rm pump} = [n(\mathrm{H_2})]^{-1} \sum_l \zeta_{{\rm pump},l} n_l , \tag{33}$$

$$\zeta_{\rm diss} = [n(\mathrm{H_2})]^{-1} \sum_l \zeta_{{\rm diss},l} n_l , \tag{34}$$

where n_l is the number density of H_2 in level l.

4.4. *Approximations for Self-Shielding*

For many purposes, it is useful to have simple analytic approximations for the dependence of the pumping rate on $N_2 \equiv N(\mathrm{H_2})$ and dust extinction $\tau_{d,1000} = N_{\rm H}\sigma_{d,1000}$. Since the dust extinction does not vary strongly over the 1110–912 Å range, the pumping rate is approximately

$$\zeta_{\rm pump}(N_2) \approx f_{\rm shield}(N_2) e^{-\tau_{d,1000}} \zeta_{\rm pump}(0) \tag{35}$$

where $f_{\rm shield}(N_2)$ represents the self-shielding effect of the H_2. Here we put forward two approximations for $f_{\rm shield}(N_2)$; their accuracy will be assessed later by comparison with detailed calculations.

A very simple power-law approximation is provided by

$$f_{\rm shield}(N_2) = \begin{cases} 1 & \text{for } N_2 < 10^{14} \text{ cm}^{-2} , \\ (N_2/10^{14} \text{ cm}^{-2})^{-0.75} & \text{for } N_2 > 10^{14} \text{ cm}^{-2} . \end{cases} \tag{36}$$

The $N_2^{-0.75}$ dependence is steeper than the $N_2^{-0.5}$ behavior expected for heavily saturated lines, but we shall see below in § 5.2 that it approximates $f_{\rm shield}$ quite well over a large range of column densities. Note, however, that this approximation behaves unphysically in the limit $N_2 \to \infty$: if there were no dust, the total pumping rate per area $\int_0^\infty \zeta_{\rm pump} dN_2 \to \infty$. This unphysical behavior corresponds to a failure to require that the total equivalent width be limited to some value $W_{\rm max} \approx 0.2$. We can correct this deficiency with a more complicated expression:

$$f_{\rm shield}(N_2) = \frac{0.965}{(1 + x/b_5)^2} + \frac{0.035}{(1 + x)^{0.5}} \times \exp[-8.5 \times 10^{-4}(1 + x)^{0.5}] , \tag{37}$$

where $x \equiv N_2/5 \times 10^{14} \text{ cm}^{-2}$, and $b_5 \equiv b/10^5 \text{ cm s}^{-1}$. This somewhat complicated functional form has been constructed so that in the absence of dust, the total pumping rate per area $\int_0^\infty \zeta_{\rm pump} dN_2 \approx \chi F$ for the $u_\nu \propto \nu^{-2}$ spectrum (24). It is also designed to reproduce the complete transition from optically thin to extreme saturation with line overlap. We shall see below that equation (37) is significantly more accurate than equation (36) yet is nevertheless straightforward to evaluate numerically and hence useful for numerical modeling.

Since the pumping rate may be written $\zeta_{\rm pump} = F_\nu dW_\nu/dN_2 = \nu F_\nu dW/dN_2$ (where $F_\nu = cu_\nu/h\nu$) and $\zeta_{\rm pump} = \zeta_{\rm pump}(0) f_{\rm shield}$, we obtain

$$W(N_2) = \Delta \ln \nu \frac{\zeta_{\rm pump}(0)}{F} \int_0^{N_2} dN_2' f_{\rm shield}(N_2') \tag{38}$$

$$= \Delta \ln \nu \times 1.05 \times \left[1 + \frac{0.0117x}{1 + x/b_5} - \exp\{-8.5 \times 10^{-4}[(1 + x)^{0.5} - 1]\}\right] , \tag{39}$$

thereby demonstrating that our assumed shielding function (37) corresponds to an equivalent width $W \approx \Delta \ln \nu \approx 0.2$ in the limit $N_2 \to \infty$. Neglecting variations in the dissociation probability $\langle p_{\rm diss} \rangle$, we may approximate the photodissociation rate by

$$\zeta_{\rm diss} \approx f_{\rm shield}(N_2) e^{-\tau_{d,1000}} \zeta_{\rm diss}(0) . \tag{40}$$

5. STRUCTURE OF STATIONARY PHOTODISSOCIATION FRONTS

5.1. *Model Assumptions*

We now consider models of stationary photodissociation fronts, in which the H_2 level populations at each point are the steady state level populations resulting from UV pumping, spontaneous radiative decay, collisional excitation and de-excitation, photodissociation, and H_2 formation on grains.

In the models presented here, we do not examine the thermal balance in the PDR. Theoretical estimates for the temperature structure of PDRs are very uncertain, pri-

marily because of uncertainties in the grain photoelectric heating: compare the temperature profiles of Tielens & Hollenbach (1985a), Burton, Hollenbach, & Tielens (1990), and Bakes & Tielens (1994). We will simply assume the kinetic temperature in the PDR to vary as

$$T = \frac{T_0}{1 + \tau_{d,1000}}, \tag{41}$$

where the initial temperature T_0 will be treated as an adjustable parameter. This temperature profile has the expected property of declining at large optical depth, as the dust grains attenuate the incident UV. The functional form is not intended to be realistic but does allow us to explore the effects of varying the gas temperature in the region in which H_2 pumping takes place.

We assume a plane-parallel geometry, with radiation propagating in the $+x$ direction. The UV intensity at $x = 0$ is specified by the parameter χ. At each point we assume an equilibrium between H_2 formation on grains and H_2 photodissociation. The H_2 level populations are similarly assumed to be in steady state statistical equilibrium. If we define

$$y_l \equiv 2n_l/n_{\rm H} \tag{42}$$

and require $\dot{y}_l = 0$, then, since $n(\mathrm{H}) = n_{\rm H}(1 - x_{\rm H} - \sum_{l=1}^{N} y_l)$, the vector y_l must satisfy the system of N inhomogeneous equations

$$\sum_{m=1}^{N} (2Rn_{\rm H}\delta_l - D_{lm})y_m = 2Rn_{\rm H}(1 - x_{\rm H})\delta_l . \tag{43}$$

As discussed in § 2, we set $x_{\rm H} = 1 \times 10^{-4}$ and include the $N = 299$ bound states of H_2 with $J \leq 29$ in our calculations. We solve for the level populations $y_m, m = 1, \ldots, N$ by LU decomposition, using routines LUDCMP and LUBKSB from Press et al. (1992). We will refer to these models as "UV-pumping" models, since the rovibrational distribution of H_2 is strongly affected by the UV pumping, and, as a result, (1) there is a significant population in rotational levels $J > 5$ that would be negligibly populated in a LTE distribution with $T_{\rm exc} \approx 100$ K and (2) the rovibrational distribution of the H_2 varies with depth in the cloud, since pumping effects are strongest near the cloud surface.

For comparison, we will also consider models in which there is a balance between H_2 photodissociation and formation on grains but where the distribution of the absorbing H_2 over rotation-vibration levels is assumed to be a thermal distribution with a specified excitation temperature $T_{\rm exc} = 100$ K. These will be referred to as "LTE" models.

5.2. *Self-Shielding*

In order to test the accuracy of our statistical treatment of line overlap, we have carried out detailed ("exact") radiative transfer calculations to compare with the photoexcitation rates computed using our statistical treatment of line overlap (eq. [30]). The "exact" calculations explicitly took into account the 900 strongest FUV absorption lines of H_2, with a fine enough frequency sampling to resolve all important frequency structure in the radiation field at different depths. This was achieved through an adaptive frequency mesh of typically 10,000 grid points and spectral resolution up to 10^6, similar to the resolution in the calculations of Abgrall et al. (1992). Another 3200 weaker lines were included using the equivalent width approximation atop the spectrum of the stronger lines. Typically, these weak lines contribute less than 5% to the total pumping rate. The CPU time–efficient transfer algorithm is part of a fully time-dependent PDR code that will be described in a forthcoming paper.

For comparison with the approximate treatment introduced in § 4.3, the H_2 level populations were assumed to be given by LTE at excitation temperature $T_{\rm exc}$. Rather than examine the actual self-shielding function, we consider the suppression of the dissociation rate, $\zeta_{\rm diss}/\zeta_{\rm diss}(0)$. We compare the dissociation rate obtained from our "exact" radiative transfer equation with $\zeta_{\rm diss}$ obtained from equation (30) for $T_{\rm exc} = 100$ K (Fig. 1) and $T_{\rm exc} = 300$ K (Fig. 2). We see that the agreement is excellent at all column densities N_2. Agreement is of course expected for low column densities $N_2 \lesssim 10^{18}$ cm^{-2}, where line overlap effects are negligible (so that treatment of the pumping as due to isolated lines is valid). This agreement persists, however, at column densities $N_2 > 10^{20}$ cm^{-2}, where line overlap effects cause $f_{\rm shield}$ to decline more rapidly than $N_2^{-0.5}$; the agreement is excellent even out to the largest column densities considered, $N_2 = 3 \times 10^{21}$ cm^{-2}, where line overlap effects suppress the pumping rates by a factor ~ 10. We have therefore validated the use of equation (30) for subsequent calculations, in which we solve for the non-LTE H_2 level populations.

For comparison with our multiline calculations, in Figures 1 and 2 we have plotted the self-shielding function for a single line in the approximation of Federman et al. (1979), with the two parameters $r = 1.3 \times 10^{-3}$ and

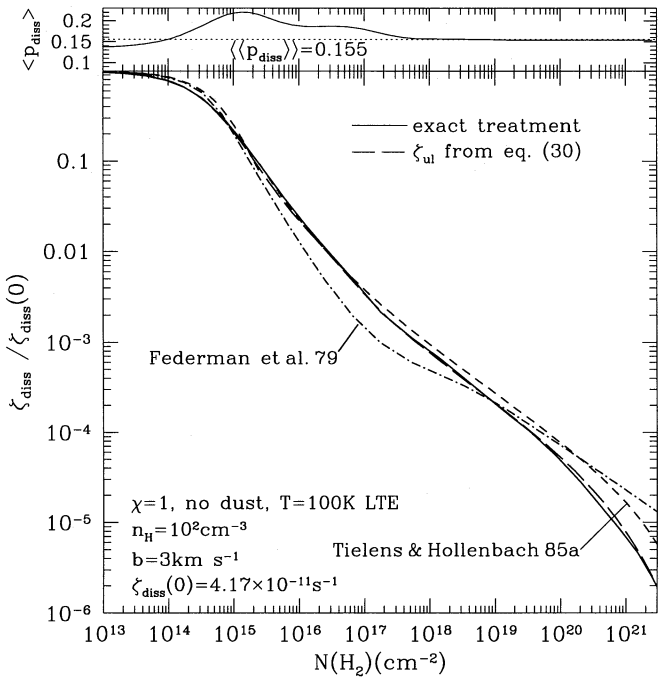

FIG. 1.—Comparison of self-shielding calculated using the statistical treatment of line overlap (eq. [30]) and an "exact" treatment of line overlap, for $T = 100$ K LTE level populations. The H_2 is assumed to have a Doppler broadening parameter $b = 3$ km s^{-1}. Models do not include dust shielding or absorption by CI. It is apparent that eq. (30) does an excellent job of accounting for line overlap. Also shown are self-shielding approximations of Federman et al. (1979) and Tielens & Hollenbach (1985a) (see text). The upper panel shows the dissociation probability $\langle p_{\rm diss}\rangle$ as a function of position; the dotted line shows the dissociation probability averaged over all UV pumping events in the PDR.

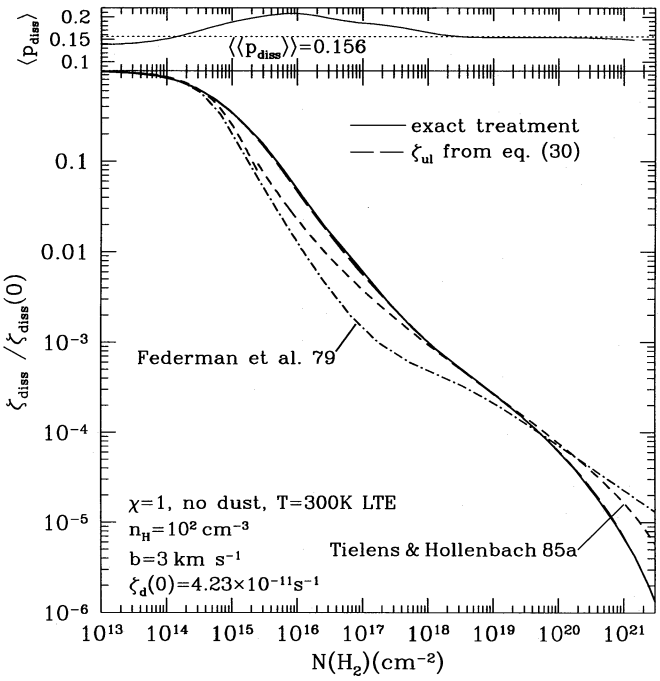

FIG. 2.—Same as Fig. 1, but for $T = 300$ K LTE populations

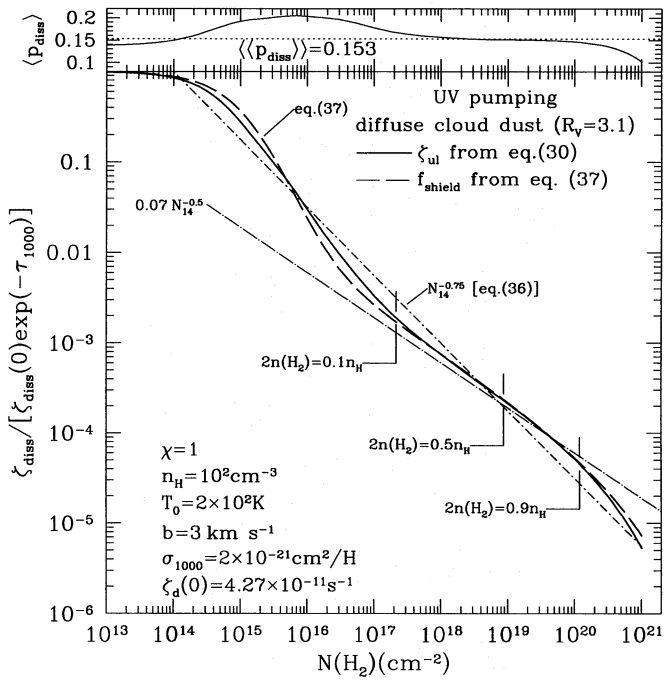

FIG. 3.—H_2 self-shielding factor f_{shield} as a function of $N(H_2)$, in a stationary photodissociation front with $\chi/n_H = 0.01$ cm^3 and $T_0 = 200$ K. The H_2 is assumed to have a Doppler broadening parameter $b = 3$ km s^{-1}. Dust absorption is included assuming diffuse cloud dust with $R_V = 3.1$. The solid line shows the dissociation rate computed from a multiline calculation with approximate treatment of line overlap, using eq. (30). The long broken line is the semianalytic fit (37). Two power-law fits are shown: $N_{14}^{-0.75}$ (eq. [36]) and a square-root fit (see text). The upper panel shows the dissociation probability $\langle p_{diss}\rangle$; the dotted line shows the dissociation probability averaged over all UV pumping events in the PDR.

$N_2/\tau_D = 10^{14.6}$ cm^{-2} chosen to match approximately the total H_2 self-shielding curve for $T_{exc} = 100$ K. It is apparent that the self-shielding of a single line is quite different from that of the total ensemble of overlapping H_2 lines. The effects of line overlap were estimated by de Jong et al. (1980); their result was used by Tielens & Hollenbach (1985a) for $N_2 \gtrsim 2 \times 10^{15}$ cm^{-2}. In Figures 1 and 2, we show the self-shielding function used by Tielens & Hollenbach. The de Jong et al. formula evidently underestimates the effects of line overlap, by approximately a factor of ~ 2.4 at $N(H_2) = 10^{21}$ cm^{-2}. Also shown in Figures 1 and 2 is the dissociation probability $\langle p_{diss}\rangle$. While $\langle p_{diss}\rangle$ varies from 0.10 to 0.21, it is generally close to the average value of ~ 0.15 (*dotted line*).

Figures 3 and 4 show the variation of the self-shielding factor for dissociation, $\zeta_{diss}/\zeta_{diss}(0)$, with depth in a cloud with $\chi/n_H = 0.01$ cm^3, for two extreme assumptions concerning the dust: diffuse cloud dust with $R_V = 3.1$ (Fig. 3) and dense cloud dust with $R_V = 5.5$ (Fig. 4). Figure 5 shows f_{shield} for dense cloud dust but with an enhanced radiation field $\chi/n_H = 0.1$ cm^3. We see in Figures 3–5 that at H_2 column density $N_2 = 1 \times 10^{21}$ cm^{-2}, the H_2 self-shielding suppresses the photodissociation rate by a factor $f_{shield} \approx 6 \times 10^{-6}$. It is also interesting to observe in Figures 3–5 the decline in $\langle p_{diss}\rangle$ at large values of N_2. This decrease (not seen in the dustless models of Figs. 1 and 2) is due to attenuation of the FUV by the dust, resulting in "reddening" of the radiation to which the H_2 is exposed, decreasing the relative importance of the photoexcitations to higher levels u, with larger values of $p_{diss,u}$.

Also plotted on Figures 3–5 is the "square root approximation" $f_{shield} \approx 7 \times 10^{-5}(10^{20}\ \text{cm}^{-2}/N_2)^{0.5}$; it is evident that except over the limited range $10^{17} \lesssim N_2 \lesssim 10^{20}$ cm^{-2}, the H_2 self-shielding function is quite different from the asymptotic $N_2^{-0.5}$ behavior which is often assumed (e.g., Hill & Hollenbach 1978; Sternberg 1988; Goldschmidt & Sternberg 1995; Hollenbach & Natta 1995). The differences arise from two effects. For $10^{15} \lesssim N_2 \lesssim 10^{17}$ cm^{-2}, the actual self-shielding function declines with increasing N_2 much more rapidly than $N_2^{-0.5}$ while many of the strongest absorbing transitions become optically thick and

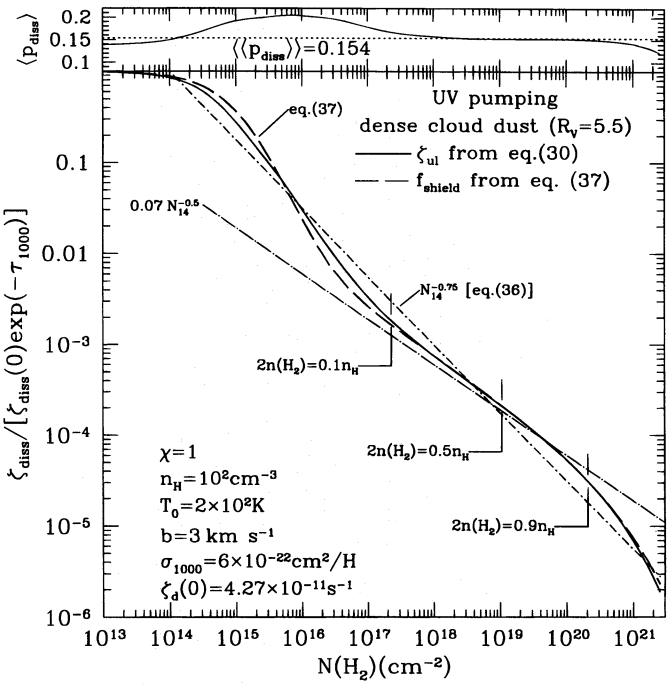

FIG. 4.—Same as Fig. 3, but for dense cloud dust with $R_V = 5.5$

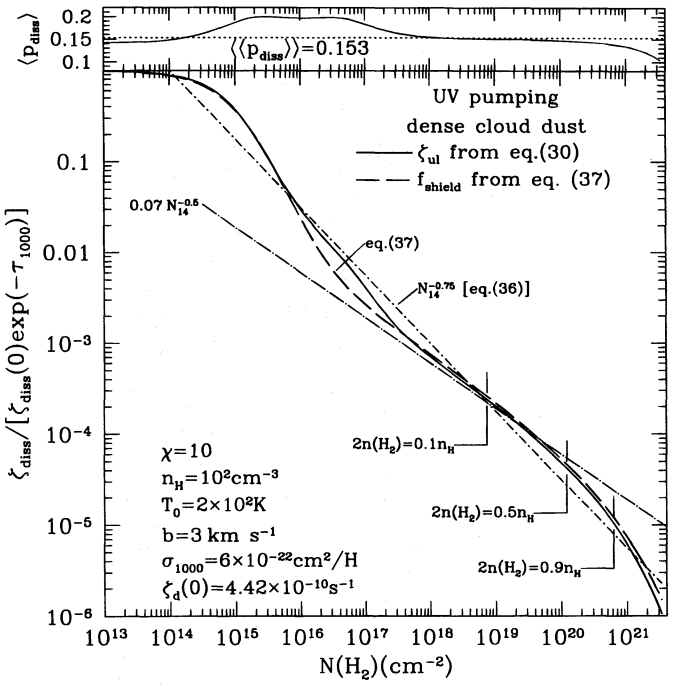

FIG. 5.—Same as Fig. 3, but for dense cloud dust and a stronger radiation field, with $\chi/n_H = 0.1$ cm^3.

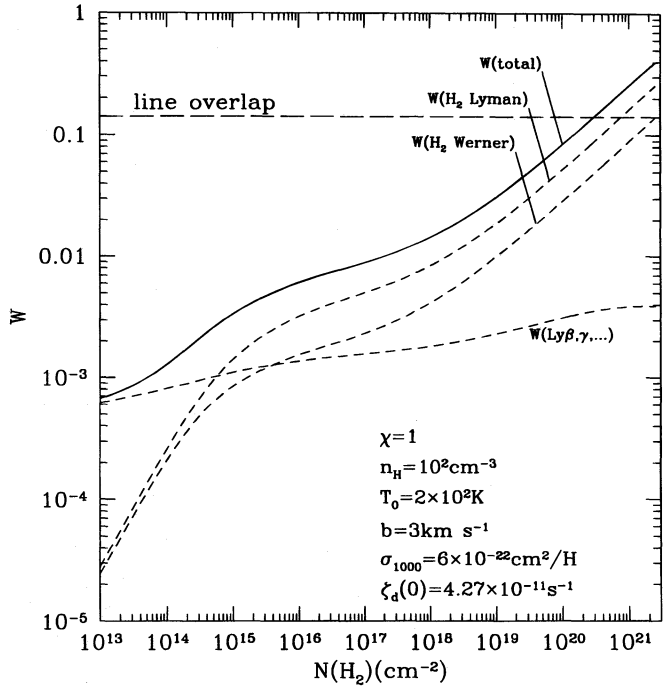

FIG. 6.—Total dimensionless equivalent width W contributed by lines in the 1110–912 Å interval, as a function of the H_2 column density, for $\chi/n_H = 0.01$ cm^3, $b = 3$ km s^{-1}, and dense cloud dust. Separate contributions of Lyman-band, Werner-band, and H I Lyman series (Lyβ through 1–15) are shown. Line overlap is expected to suppress pumping rates by a factor ~ 2 when W(total) equals $0.2 \ln(2) = 0.14$; this occurs at $N(H_2) = 3 \times 10^{20}$ cm^{-2}.

enter the "flat" portion of the curve of growth. The column density range of this steep drop is wider than that of a single line because initially less important transitions (i.e., those with smaller oscillator strength and/or smaller populations) are still optically thin and increase in relative importance when the stronger lines become saturated. Only at $N_2 > 10^{17}$ cm^{-2} have all important pumping lines reached the square root part of the curve of growth. For $N_2 \gtrsim 10^{20}$ cm^{-2}, f_{shield} falls off more rapidly than $N_2^{-0.5}$ as the result of line overlap. The function $7 \times 10^{-5}(10^{20}\ \text{cm}^{-2}/N_2)^{0.5}$ underestimates f_{shield} by a factor ~ 20 at $N_2 = 10^{15}$ cm^{-2} and overestimates f_{shield} by a factor ~ 4 at $N_2 = 10^{21}$ cm^{-2}.

The importance of line overlap is shown by Figure 6, where we plot the total equivalent width W summed over Lyman and Werner series for H_2, plus the H Lyman series from Lyβ through H1–15. Treating the frequencies of the lines in the 1110–912 Å band as independent random variables, our statistical treatment of line overlap, with $f_{shield} \propto \exp(-W/0.2)$, gives a factor of 2 suppression of f_{shield} when the total equivalent width $W = 0.2 \ln(2) = 0.14$, which occurs for $N_2 \approx 3 \times 10^{20}$ cm^{-2} (see Fig. 6)

If a power-law fit to the self-shielding factor f_{shield} is desired, the $N_2^{-3/4}$ power law of equation (36), shown in Figures 3–5, seems most suitable; it succeeds in reproducing f_{shield} to within a factor of 2 for $10^{14} < N_2 < 5 \times 10^{20}$ cm^{-2}.

If a more accurate approximate representation of f_{shield} is desired, we favor equation (37), also shown in Figures 3–5. This functional form does an excellent job in reproducing the initial rapid decline in f_{shield} for $10^{14} < N_2 < 10^{17}$ cm^{-2}, the "square root" behavior for $10^{17} < N_2 < 10^{20}$ cm^{-2}, and the rapid falloff due to line overlap for $N_2 > 10^{20}$ cm^{-2}.

As already seen from comparison of Figures 1 and 2, the detailed dependence of f_{shield} on N_2 depends upon the rovibrational distribution of the absorbing H_2. In Figure 7 we compare f_{shield} computed for (1) an LTE ($T_{exc} = 100$ K) H_2 level distribution (see Fig. 1), (2) a non-LTE rovibrational distribution due to UV pumping with $\chi = 1$ and collisional excitation/de-excitation with $n_H = 10^2$ cm^{-3} and $T = 100$

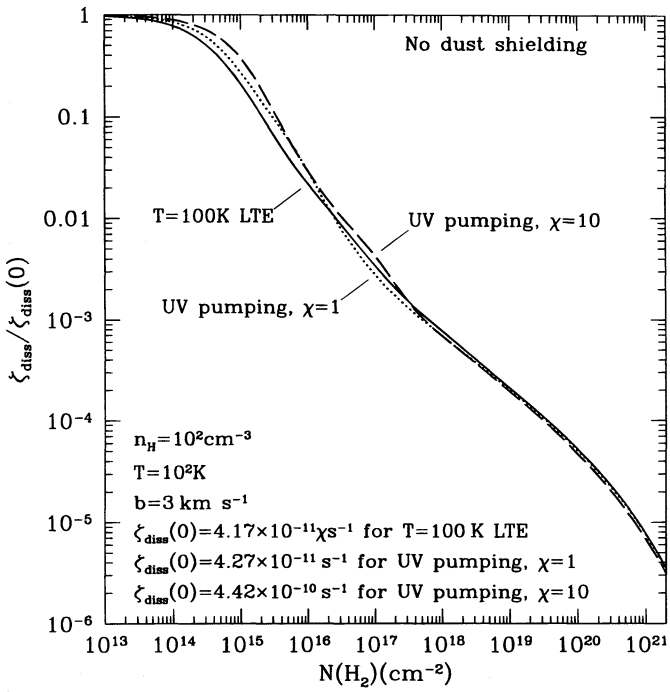

FIG. 7.—Self-shielding for three photodissociation fronts: $T = 100$ K LTE level populations (*solid line*), and UV pumping with $\chi = 1$ (*dotted*) and $\chi = 10$ (*broken*) (with $n_H = 10^2$ cm^{-3} and $T = 10^2$ K). It is seen that the three self-shielding factors are essentially identical for $N(H_2) \gtrsim 2 \times 10^{17}$ cm^{-2}.

K (see Fig. 4), and (3) same as (2), but with $\chi = 10$ (see Fig. 5). In order to bypass any questions related to dust opacities, the plots in Figure 7 are for cases with zero dust extinction. We see that for $10^{14} \lesssim N_2 \lesssim 10^{18}$ cm^{-2}, $f_{\rm shield}$ does show a dependence on the details of the H_2 rovibrational distribution. When there is higher excitation, the pumping occurs via a larger number of lines, so that the H_2 remains optically thin a bit longer, and self-shielding is less effective until one enters the heavily damped regime at $N_2 \gtrsim 10^{18}$ cm^{-2}. Overall, however, the self-shielding function $f_{\rm shield}(N_2)$ is relatively insensitive to the effects of UV pumping with $\chi \lesssim 10^3$.

Figure 8 shows profiles of the fractional abundance of H_2 as a function of total column density $N_{\rm H}$ for five different values of $\chi/n_{\rm H}$ ($=10^{-3}$, 0.01, 0.1, 1, and 10 cm^3) and two different dust opacity laws ($R_V = 3.1$ and 5.5). As the radiation intensity to density ratio $\chi/n_{\rm H}$ is raised, the column density of atomic, dusty gas increases.

In Figures 9 and 10, we show the run of $N(H_2)$ versus $N_{\rm H}$ for models parameterized by $\chi/n_{\rm H}$. Models assuming diffuse cloud dust properties are shown in Figure 9; dense cloud dust is considered in Figure 10. The region in which line overlap is important is shown in each figure, as is the region in which attenuation of the UV by dust is significant. It is seen from Figure 10 that line overlap plays an important role in self-shielding. For example, a dense cloud dust model with $\chi/n_{\rm H} = 0.01$ cm^3 has line overlap suppressing the dissociation rate by factors of 2–4 at column densities $5 \lesssim N_{\rm H} \lesssim 12 \times 10^{20}$ cm^{-2}, where dust extinction attenuates the radiation field by less than a factor of 2.

The 1–0 $S(1)$ line originates from $H_2(v = 1, J = 3)$. In Figure 11, we show the column density of this excited state, divided by χ, as a function of the total column density $N_{\rm H}$, so that one can see how deep into the cloud one must go to account for most of the 1–0 $S(1)$ line emission. For each case we indicate the "median" for 1–0 $S(1)$ emission: the loca-

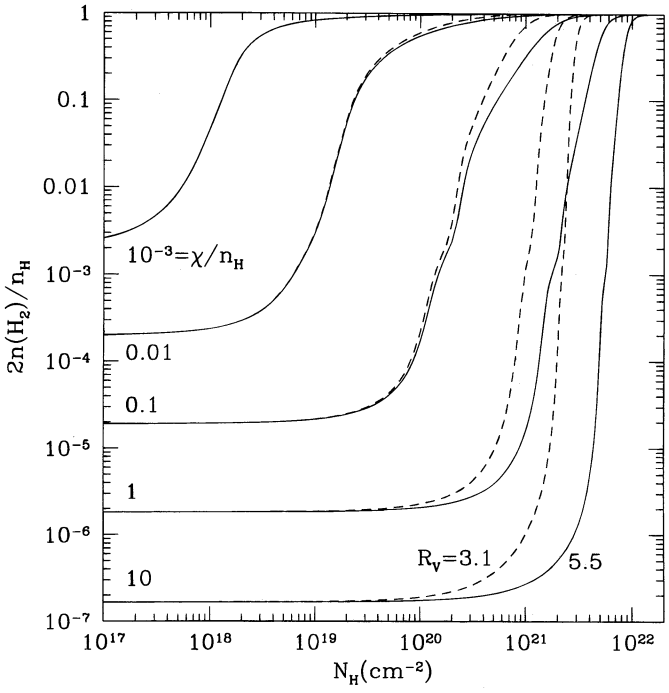

FIG. 8.—H_2 fractions in stationary, plane-parallel photodissociation fronts for $n_{\rm H} = 10^2$ cm^{-3} and $T_0 = 200$ K, for selected values of $\chi/n_{\rm H}$ (cm^3) and dust with $R_V = 3.1$ ($\sigma_{d,1000} = 2 \times 10^{-21}$ cm^2) and $R_V = 5.5$ ($\sigma_{d,1000} = 6 \times 10^{-22}$ cm^2). $\lambda > 912$ Å radiation with $u_\nu \propto \nu^{-2}$ is propagating in the $+x$ direction at $N_{\rm H} = 0$. $N_{\rm H}$ is the total column density of H nucleons. Self-shielding of the H_2 is computed for 27,983 lines using eq. (30) with $W_{\rm max} = 0.2$.

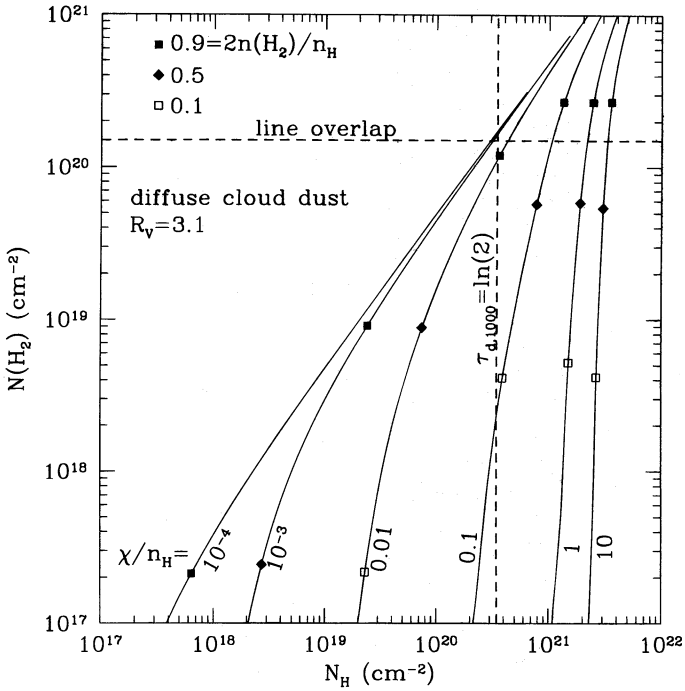

FIG. 9.—$N(H_2)$ vs. $N_{\rm H}$ for photodissociation fronts with diffuse cloud dust. Models are labeled by $\chi/n_{\rm H}$ (cm^3). Calculations were done for $n_{\rm H} = 10^2$ cm^{-3}, $T_0 = 200$ K. Line overlap contributes more than a factor of 2 to the self-shielding above the horizontal line. To the right of the vertical line, dust shielding contributes more than a factor of 2. Points on each curve show locations at which the H_2 fraction is 0.1, 0.5, and 0.9. It is seen that for diffuse cloud dust properties, dust shielding is important whenever line overlap occurs.

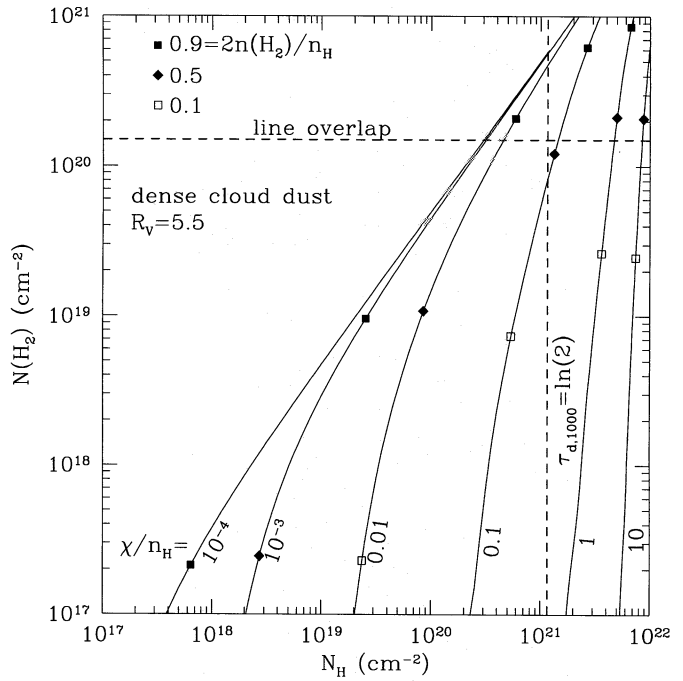

FIG. 10.—Same as Fig. 9, but for dense cloud dust. It is seen that line overlap can be important even when dust absorption plays a minor role (e.g., $\chi/n_{\rm H} = 0.01$ cm^3 and $N_{\rm H} = 5 \times 10^{20}$ cm^{-2}). Calculations were done with $n_{\rm H} = 10^2$ cm^{-3}, $T_0 = 200$ K.

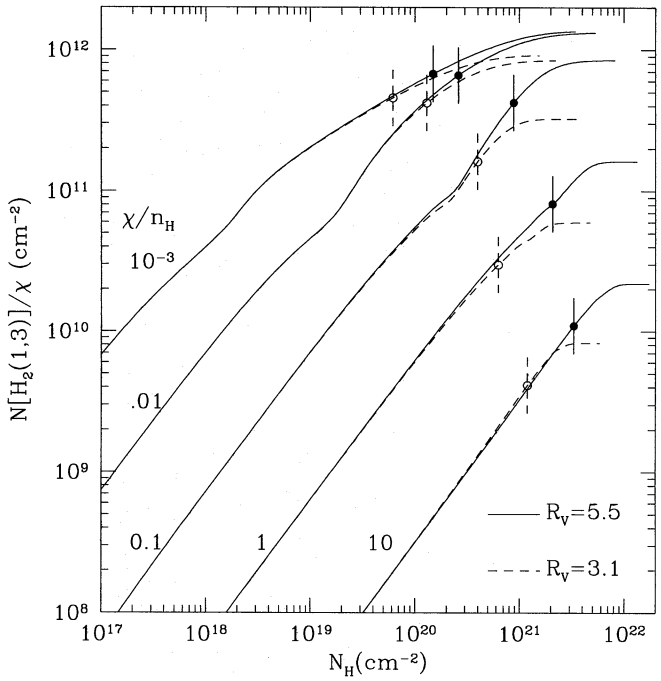

FIG. 11.—Column density of H_2 ($v = 1$, $J = 3$) divided by χ in stationary, plane-parallel photodissociation fronts, labeled by χ/n_H (cm^3), for dust with $R_v = 3.1$ and 5.5 . N_H is the total column density of H nucleons. Self-shielding of the H_2 is computed using eq. (30) with $W_{max} = 0.2$. Calculations were done for $n_H = 10^2$ cm^{-3}, $T_0 = 200$ K. Results are valid for $\chi \lesssim 2000$ and $n_H \lesssim 10^5$ cm^{-3} (so that UV pumping and collisional deexcitation out of vibrationally excited levels are slower than spontaneous decay). For each case, a vertical line indicates the "median" location for 1–0 $S(1)$ emission (see text).

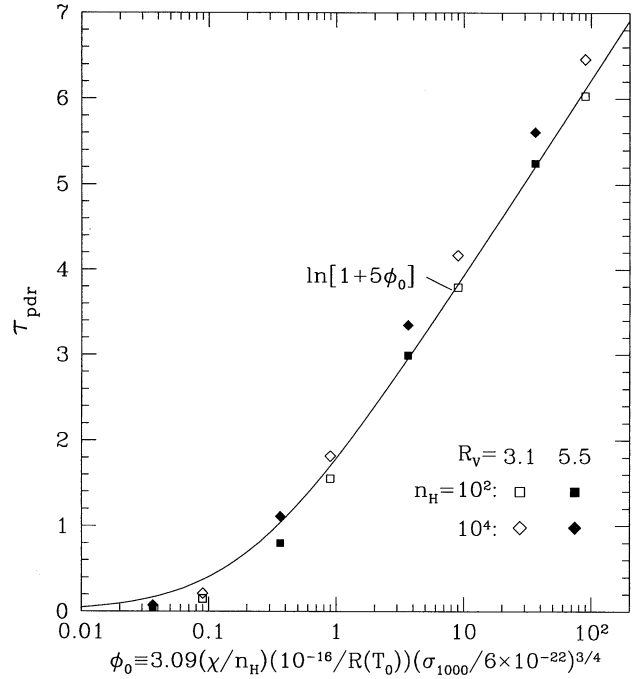

FIG. 12.—Dust optical depth τ_{pdr} at $\lambda = 1000$ Å between the ionization front and the point at which $2n(H_2) = n(H)$, as a function of the dimensionless parameter ϕ_0. Results are shown for two different extinction laws. It is seen that τ_{pdr} may be approximated by $\tau_{pdr} \approx \ln(1 + 5\phi_0)$. Numerical results are for $T_0 = 200$ K.

tion at which 50% of the 1–0 $S(1)$ emission occurs on either side. For $\chi/n_H = 10^{-3}$ cm^3, the 1–0 $S(1)$ median is at $N_H = 1.5 \times 10^{20}$ cm^{-2}, but for $\chi/n_H = 0.1$ cm^3, for example, the 1–0 $S(1)$ median is at $N_H = 8.5 \times 10^{20}$ cm^{-2} (for $R_V = 5.5$ dust).

5.3. *Width of the PDR*

To assess the importance of shielding by dust, it is useful to define the dust optical depth of the PDR, τ_{pdr}, which we take to be the dust optical depth at $\lambda = 1000$ Å measured to the point at which 50% of the local hydrogen is molecular: $2n(H_2)/n_H = 0.5$. In Figure 12, we plot τ_{pdr} as a function of the parameter ϕ_0 defined in Bertoldi & Draine (1996):

$$\phi_0 \equiv 25.4\left(\frac{\chi\ \text{cm}^{-3}}{n_H}\right) \times \left[\frac{3 \times 10^{-17}\ \text{cm}^3\ \text{s}^{-1}}{R(T_0)}\right]\left(\frac{\sigma_{d,1000}}{2 \times 10^{-21}\ \text{cm}^2}\right)^{3/4}, \quad (44)$$

where the rate coefficient R for H_2 formation on grains is evaluated at temperature T_0. For R given by equation (18), this becomes

$$\phi_0 = 5.15\left(\frac{\chi\ \text{cm}^{-3}}{n_H}\right)\left(\frac{100\ \text{K}}{T_0}\right)^{1/2}\left(\frac{\sigma_{d,1000}}{6 \times 10^{-22}\ \text{cm}^2}\right)^{3/4}. \quad (45)$$

We see that shielding by dust is important ($\tau_{pdr} > 1$) for $\phi_0 > 0.5$ but relatively unimportant for $\phi_0 < 0.1$. A good fit to the numerical results is provided by the simple fitting function (see Fig. 12)

$$\tau_{pdr} \approx \ln(1 + 5\phi_0)\,. \quad (46)$$

5.4. *Pumping Efficiency*

Because of the increased importance of dust for large ϕ_0, the efficiency of conversion of incident UV into H_2 fluorescence is reduced. One measure of this is the "pumping efficiency," the ratio

$$\epsilon_{pump} = \frac{\int \zeta_{pump}\, dN_2}{F}\,, \quad (47)$$

where F is the incident flux of 1110–912 Å photons (see eq. [21]). Since there is only a minor contribution to pumping by $\lambda > 1110$ Å photons, ϵ_{pump} is essentially the fraction of the incident 1110–912 Å photons that are absorbed by H_2, rather than dust, so that the H_2 dissociation rate/area and (for $n_H \lesssim 10^4$ cm^{-3}) the fluorescent surface brightness of the cloud are proportional to $\epsilon_{pump} F \propto \epsilon_{pump} \chi$.

In Figure 13 we plot ϵ_{pump} versus the parameter ϕ_0 for models with $T_0 = 200$ K but with a variety of densities and both diffuse cloud dust and dense cloud dust. We see that $\epsilon_{pump} \approx 0.5$ for $\phi_0 \lesssim 0.1$. Strictly speaking, ϵ_{pump} is a function of both $\chi/n_H R$ and σ_d,[6] but we find that the pumping efficiency ϵ_{pump} can in practice be approximated as depend-

[6] It is clear, for example, that for $\sigma_d \to 0$ (in which case $\phi_0 \to 0$) we should have $\epsilon_{pump} \approx 1$ since all 1110–912 Å photons must eventually be absorbed by H_2 (neglecting the H Lyman lines and CI absorption). However, for values of σ_d and ϕ_0 of practical interest, we find that $\epsilon_{pump} \approx 0.5$ for $\phi_0 \ll 1$.

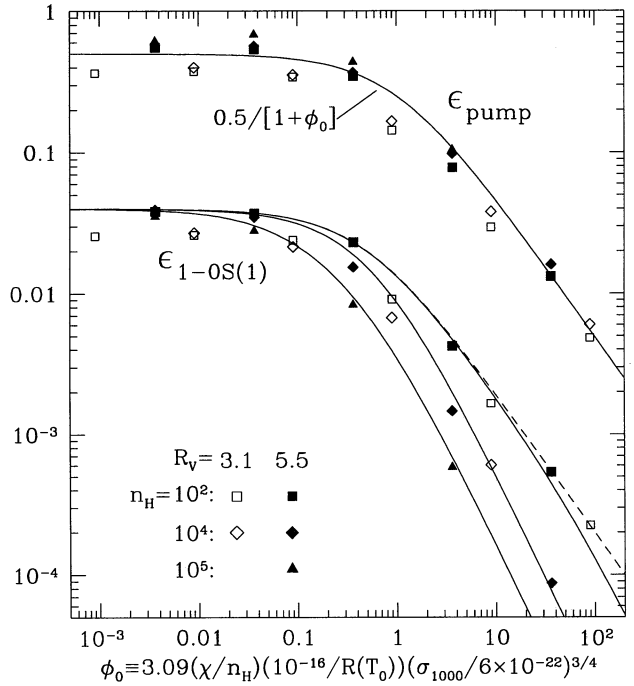

FIG. 13.—The UV pumping efficiency ϵ_{pump}, the fraction of incident 1110–912 Å photons which are absorbed by H_2 rather than dust, and $\epsilon_{1-0\,S(1)}$, the number of 1–0 $S(1)$ photons emitted per incident 1110–912 Å photon. Numerical results are for $T_0 = 200$ K. The estimate (48) for ϵ_{pump} is shown as a solid curve. The estimate (50) for $\epsilon_{1-0\,S(1)}$ is shown for dense cloud dust with $R(T_0) = 8.46 \times 10^{-17}$ cm^3 s^{-1} for $n_H \to 0$ (*broken curve*) and for $n_H = 10^2$, 10^4, and 10^5 cm^{-3} (*solid curves*).

ing on the single parameter ϕ_0, with the fitting function

$$\epsilon_{pump} \approx \frac{0.5}{1+\phi_0} \tag{48}$$

providing a reasonable fit to our results (see Fig. 13). Also shown in Figure 13 is the "efficiency" $\epsilon_{1-0\,S(1)}$ for emission of the strong 1–0 $S(1)$ line. We define this in terms of the surface brightness $I[1 \to 0\ S(1), \theta = 0]$ measured normal to the PDR (and including the effects of internal dust; see eq. [53]):

$$\epsilon_{1-0\,S(1)} \equiv \frac{4\pi I[1 \to 0\ S(1), \theta = 0]}{hc/\lambda_{1-0\,S(1)}} \frac{1}{F} . \tag{49}$$

Provided that $n_H \lesssim 10^5$ cm^{-3} [so that collisional de-excitation does not compete with spontaneous decay out of (1, 3)], we find that $\epsilon_{1-0\,S(1)}$ may be approximated by

$$\epsilon_{1-0\,S(1)} \approx \frac{0.04}{1+2\phi_0} \frac{1}{[1+(\chi/2000)^{0.5}]} , \tag{50}$$

showing that for $\phi_0 \lesssim 0.1$ and $\chi \lesssim 2000$, $\epsilon_{1-0\,S(1)} \approx 0.08\epsilon_{pump}$: ~8% of the UV pumping events result in fluorescent emission of a 1–0 $S(1)$ photon. Thus, for $n_H \lesssim 10^5$ cm^{-3},

$$I[1 \to 0\ S(1), \theta = 0] \approx \frac{3.6 \times 10^{-8}\chi}{(1+2\phi_0)[1+(\chi/2000)^{0.5}]} \text{ ergs cm}^{-2}\text{ s}^{-1}\text{ sr}^{-1} . \tag{51}$$

Unlike ϵ_{pump}, we see from Figure 13 that $\epsilon_{1-0\,S(1)}$ is not determined solely by ϕ_0 but also shows sensitivity to the actual values of n_H and χ when $n_H \gtrsim 10^5$ cm^{-3} or $\chi \gtrsim 10^3$. This is because at high densities or high intensities, (1) the rotational population is changed, affecting the probability of populating the $v = 1$, $J = 3$ level, and (2) collisional de-excitation (at $n_H \gtrsim 10^5$ cm^{-3}) or radiative pumping (at $\chi \gtrsim 10^3$) may act to depopulate the $v = 1$, $J = 3$ level. For $n_H \lesssim 10^5$ cm^{-3} we find that equation (50) provides a good estimate for the intensity of the 1–0 $S(1)$ line.

6. FLUORESCENT EMISSION SPECTRA

6.1. *Effects of Internal Extinction*

The true column density in level (v, J) along a line making an angle θ with respect to the normal is simply

$$N(v, J) = \frac{1}{\cos(\theta)} \int_0^\infty dx\, n(v, J) . \tag{52}$$

The emission in vibration-rotation lines of H_2 is

$$I(u \to l, \theta) = \frac{1}{\cos(\theta)} \int_0^\infty dx\, \frac{A_{lu}}{4\pi} n_u \frac{hc}{\lambda_{ul}} \times \exp\left[\frac{-N_H(x)\sigma(\lambda_{ul})}{\cos(\theta)}\right], \tag{53}$$

where θ is the angle of inclination of the front as seen by the observer and where we have allowed for absorption of the fluorescent emission by dust within the photodissociation front [$N_H(x) = \int_0^x dx' n_H(x')$].

When a surface brightness $I_{obs}(v, J \to v', J')$ is observed in an H_2 transition $v, J \to v', J'$, one may directly compute the "apparent" column density $N_{app}(v, J)$ in the upper level from

$$N_{app}(v, J) = \frac{4\pi\lambda_{ul} I_{obs}(v, J \to v', J')}{hcA(v, J \to v', J')} . \tag{54}$$

Because of extinction, however, the true column density is larger. It is usual to infer an "observed" or "dereddened" column density

$$N_{obs}(v, J) = N_{app}(v, J) 10^{0.4A_\lambda} , \tag{55}$$

where A_λ is the estimated extinction, in magnitudes, at the wavelength λ of the observed transition $v, J \to v', J'$.

6.2. *Sensitivity of the PDR to Incident Spectrum*

PDRs may be produced by radiation from stars ranging from late B-type to early O-type, and the properties of the PDR will in principle depend upon the color temperature of the illuminating radiation as well as on χ, measuring the intensity at 1000 Å. Figure 14 shows $\epsilon_{1-0\,S(1)}$ and selected line ratios for a series of PDR models in which χ and n_H are held constant but the illuminating radiation is taken to be a dilute blackbody with color temperature $T_{color} = 10{,}000$ K (A0 spectrum) to $T_{color} = 40{,}000$ K (O4 spectrum). The models have $\chi = 10^3$ and $n_H = 10^4$ cm^3—for this density, collisional de-excitation is relatively unimportant for vibrationally excited levels, so that the emission from these models should show maximum sensitivity to the spectrum of the illuminating radiation. We see, however, that the emission properties of the PDR are essentially independent of T_{color} for $T_{color} > 12{,}000$ K. This insensitivity allows us to limit our study to models computed for power-law spectra with $\alpha = -2$ (corresponding to $T_{color} = 29{,}000$ K) and apply them to PDRs produced by a broad range of star types.

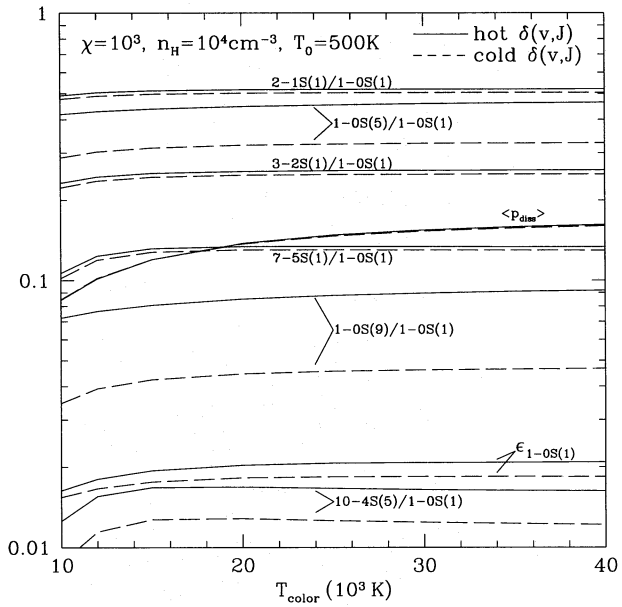

FIG. 14.—Selected line intensity ratios for $\chi = 10^3$, $n_H = 10^4$ cm^{-3}, vs. the color temperature T_{color} of the incident radiation field. Curve labeled $\epsilon_{1-0\,S(1)}$ is the efficiency for 1–0 $S(1)$ line emission [eq. (49)]. Solid and broken curves are, respectively, for newly formed H_2 that is rovibrationally "hot" ($T_f = 5 \times 10^4$ K) and "cold" ($T_f = 2000$ K). The PDR is assumed to have $T_0 = 500$ K, dust with $R_V = 5.5$, $\sigma_{d,1000} = 6 \times 10^{-22}$ cm^2, and H_2 formation rate given by eq. (18). Line ratios are seen to be essentially independent of T_{color} for $T_{color} \gtrsim 12{,}000$ K. Intensities of lines out of levels (v, J) with $J = 3$ [$S(1)$ lines] are essentially independent of the value of T_f. Intensities of lines out of levels with $J = 7$ [$S(5)$ lines] are increased by $\sim 50\%$ when T_f is varied from 2000 K to 5×10^4 K. Intensities of lines out of levels with $J = 11$ [$S(9)$ lines] are a factor of ~ 2 stronger when the newly formed H_2 is "hot" rather than "cold."

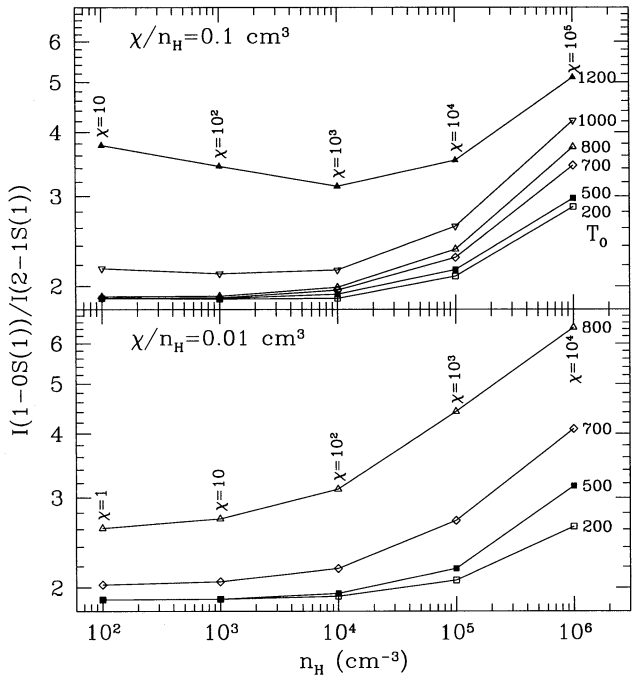

FIG. 15.—1–0 $S(1)$/2–1 $S(1)$ intensity ratio vs. density n_H. The dust is assumed to have $R_V = 5.5$, $\sigma_{d,1000} = 6 \times 10^{-22}$ cm^2, and $R(T)$ from eq. (18). Curves are labeled by T_0 (see eq. [41]). For pure fluorescence ($n_H \ll 10^5$ cm^{-3} and $T_0 \ll 500$ K), we have 1–0 $S(1)$/2–1 $S(1) = 1.9$; collisional effects increase the ratio by collisional excitation of $v = 1$ and preferential de-excitation of $v = 2$.

6.3. *Sensitivity to $\delta(v, J)$ for Newly Formed H_2*

In Figure 14, we also investigate the sensitivity of the emission spectrum to the assumed distribution function $\delta(v, J)$ of newly formed H_2. The solid curves are for models with "hot" H_2, with $T_f = 5 \times 10^4$ K, and the broken curves are for models with "cold" H_2, with $T_f = 2000$ K. We see that the intensities of lines out of levels with low J [e.g., $S(1)$ lines out of $J = 3$] are essentially unaffected by the assumed properties of δ, even for high vibrational levels [e.g., 7–5 $S(1)$]. Lines out of levels with higher J values show increasing sensitivity to the assumed δ: $S(5)$ lines out of $J = 7$ levels vary by about 40% between models with hot or cold H_2, and $S(9)$ lines out of $J = 11$ levels are about a factor of ~ 2 stronger in models with hot H_2 versus cold H_2.

It is interesting to note that the sensitivity to the assumed $\delta(v, J)$ is primarily determined by the J value of the upper state and seems not to depend particularly on the value of v: the 10–4 $S(5)$ line and the 1–0 $S(5)$ line each increase by about 50% as the newly formed H_2 is changed from "cold" to "hot." Unfortunately, as we show below, the rotational distribution of the H_2 depends on χ, n_H, and the gas temperature; unless these other properties of the PDR are known quite accurately, it does not seem likely that we will be able to use observations of PDR emission spectra to determine the distribution function $\delta(v, J)$ of newly formed H_2.

6.4. *1–0 $S(1)$/2–1 $S(1)$ Line Ratio*

The 1–0 $S(1)$/2–1 $S(1)$ line ratio is frequently used to characterize H_2 line-emitting regions. In Figure 15, we show this intensity ratio (for PDRs viewed face-on) as a function of gas density n_H, and a number of values of the temperature T_0 (see eq. [41]). Results are shown for two different values of the ratio χ/n_H. At low densities and temperatures, the line ratio (for $u_v \propto v^{-2}$, or $T_{color} \approx 3 \times 10^4$ K) is I[1–0 $S(1)$]/I[2–1 $S(1)$] = 1.9, reflecting excitation by radiative pumping, with negligible collisional de-excitation (or radiative excitation) out of vibrationally excited levels. As seen from Figure 14, the line ratio is insensitive to the value of T_{color}.

As the temperature and density are increased, two effects occur: collisional de-excitation and collisional excitation. Collisional de-excitation out of the $v = 2$ (and higher) levels acts to reduce the intensity of 2–1 $S(1)$ emission; while collisional de-excitation also depopulates the $v = 1$ levels, the rate coefficients for de-excitation out of $v = 2$ levels (by collisions with H; Martin & Mandy 1995) are significantly larger than those for de-excitation out of $v = 1$; hence, collisional de-excitation tends to raise the 1–0 $S(1)$/2–1 $S(1)$ line ratio.

If the temperature is high enough, collisional excitation of the $v = 1$, $J = 3$ level can also become important. For $\chi/n_H = 0.01$ cm^3 and $n_H \lesssim 10^4$ cm^{-3}, collisional excitation contributes $\sim 5\%$ of the 1–0 $S(1)$ emission for $T_0 = 700$ K, $\sim 30\%$ of the 1–0 $S(1)$ emission for $T_0 = 800$ K and dominates the 1–0 $S(1)$ emission for $T_0 \gtrsim 850$ K.

As χ/n_H increases, collisional excitation becomes relatively less important (at fixed T_0) for two reasons: First of all, our adopted temperature profile (eq. [41]) has the highest temperature in the region in which the H_2 abundance is low. In the optically thin region, the H_2 fraction is proportional to n_H/χ, so that increasing χ/n_H decreases the amount of H_2 present in the hottest part of the PDR (e.g.,

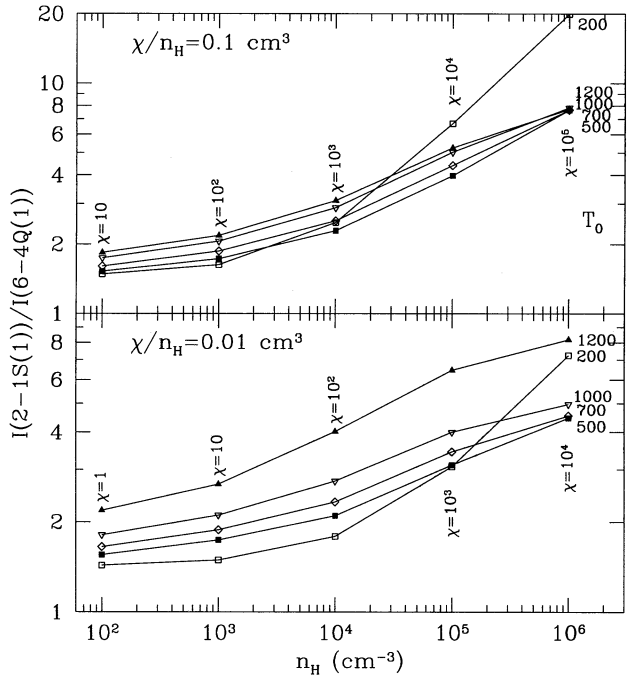

FIG. 16.—As in Fig. 15, but for the 2–1 $S(1)/6$–4 $Q(1)$ intensity ratio. The line ratio is affected by the rotational distribution of the H_2 [which explains why the line ratio depends upon T_0 even for $n_H = 10^2$ cm^{-3}], and upon the effects of collisional de-excitation of $(v, J) = (2, 3)$ and (6, 1).

where $0.8T_0 < T < T_0$). Second, when χ/n_H is increased, τ_{pdr} increases (see Fig. 12). For our assumed temperature profile (eq. [41]), this implies a reduction in T at the location at which $2n(H_2) = n(H)$, thereby decreasing the rate of collisional de-excitation. Therefore, when χ/n_H is increased, collisional excitation of 1–0 $S(1)$ does not become important until higher temperatures: for $\chi/n_H = 0.1$ cm^3, we see that for $T_0 = 1000$ K, the collisional excitation contributes only $\sim 10\%$ of the 1–0 $S(1)$ emission and only begins to dominate for $T_0 \gtrsim 1200$ K.

6.5. *2–1 S(1)/6–4 Q(1) Line Ratio*

The 6–4 $Q(1)$ line ($\lambda = 1.6015$ μm) is sufficiently strong for spectroscopic measurement (see, e.g., Luhman & Jaffe 1996), and the 2–1 $S(1)/6$–4 $Q(1)$ line ratio is a useful indicator of conditions in the region in which UV pumping is taking place. Whereas the 2–1 $S(1)/1$–0 $S(1)$ line ratio can be affected by collisional excitation of (1, 3) ($E/k = 6951$ K), the 2–1 $S(1)/6$–4 $Q(1)$ line ratio is much less sensitive to collisional excitation because the (2, 3) level has $E/k = 12{,}550$ K). The 2–1 $S(1)/6$–4 $Q(1)$ ratio is therefore a relatively direct probe of collisional de-excitation of (6, 1) versus (2, 3).

The dependence of the 2–1 $S(1)/6$–4 $Q(1)$ line ratio on the density n_H and temperature profile parameter T_0 is shown in Figure 16. Because the 2–1 $S(1)$ line originates from $J = 3$ while the 6–4 $Q(1)$ line originates from $J = 1$, the line ratio

TABLE 3

LIBRARY OF STATIONARY PDR MODELS[a]

Model	n_H (cm^{-3})	χ[b]	$\sigma_{d,1000}$ (10^{-22} cm^2)	T_0[c] (K)	cos θ[d]	I[1–0 S(1)] (ergs cm^{-2} sr^{-1} s^{-1})
am3d.....	10^2	1	20	300	1	2.16×10^{-8}
am3o.....	10^2	1	6	300	1	3.38×10^{-8}
aw3d.....	10^2	1	20	500	1	2.41×10^{-8}
aw3o.....	10^2	1	6	500	1	3.70×10^{-8}
bw3d.....	10^2	10	20	500	1	1.18×10^{-7}
bw3o.....	10^2	10	6	500	1	2.36×10^{-7}
bh3d.....	10^2	10	20	1000	1	1.50×10^{-7}
bh3o.....	10^2	10	6	1000	1	3.30×10^{-7}
Bm3o.....	10^3	10	6	300	1	3.54×10^{-7}
Bw3o.....	10^3	10	6	500	1	3.92×10^{-7}
Cw3o.....	10^3	10^2	6	500	1	2.36×10^{-6}
Ch3o.....	10^3	10^2	6	1000	1	3.08×10^{-6}
Gm3o.....	10^4	10^2	6	300	1	3.41×10^{-6}
Gw3o.....	10^4	10^2	6	500	1	3.65×10^{-6}
Hw3o.....	10^4	10^3	6	500	1	1.85×10^{-5}
Hh3o.....	10^4	10^3	6	1000	1	2.20×10^{-5}
Lm3o.....	10^5	10^3	6	300	1	2.61×10^{-5}
Lw3o.....	10^5	10^3	6	500	1	2.69×10^{-5}
Mw3o.....	10^5	10^4	6	500	1	9.66×10^{-5}
Mh3o.....	10^5	10^4	6	1000	1	1.17×10^{-4}
Qm3o.....	10^6	10^4	6	300	1	1.32×10^{-4}
Qw3o.....	10^6	10^4	6	500	1	1.42×10^{-4}
Rw3o.....	10^6	10^5	6	500	1	3.86×10^{-4}
Rh3o.....	10^6	10^5	6	1000	1	4.66×10^{-4}
n2023a.....	10^5	5000	6	500	0.2	3.29×10^{-4}
n2023b.....	10^5	5000	6	900	0.2	4.04×10^{-4}

[a] Models available via anonymous ftp from astro.princeton.edu, subdirectory draine/pdr, or at http://www.astro.princeton.edu/ ~ draine/ . All models have $b = 3$ km s^{-1}, newly formed H_2 with $T_f = 5 \times 10^4$ K, and incident UV with $u_\nu \propto \nu^{-2}$.

[b] UV intensity; see eq. (20).

[c] Parameter determining temperature profile via eq. (41).

[d] θ = viewing angle.

depends on the gas temperature even at low densities where collisional de-excitation of the levels is negligible: the line ratio increases with increasing T_0 at low densities. When the gas density is high enough that collisional de-excitation begins to compete with radiative decay of the $(v, J) = (6, 1)$ level, the line ratio increases, since the collisional rate coefficients (Martin & Mandy 1995) are such that the (6, 1) level is more strongly affected than the (2, 3) level. At the highest density $n_H = 10^6$ cm^{-3}, we obtain very high values of 2–1 $S(1)$/6–4 $Q(1)$ when $T_0 = 200$ K (see Fig. 16). At these high densities, the relative strengths of 2–1 $S(1)$ and 6–4 $Q(1)$ are primarily determined by the relative rates of collisional de-excitation of (2, 3) and (6, 1) by atomic H. We remind the reader that we use an uncertain extrapolation of the results of Martin & Mandy (1995) to low temperatures (see eq. [16]). For the temperatures $T < 200$ K in our $T_0 = 200$ K models, these extrapolated rates are *very* uncertain; we have included these models mainly to show that extreme values of the 2–1 $S(1)$/6–4 $Q(1)$ line ratio are possible at high densities. Reliable calculations of line ratios for high-density, low-temperature models will not be possible until accurate inelastic cross sections are available for low energies, requiring quantal calculations and an accurate potential surface.

6.6. *Models*

A PDR has hundreds of fluorescent emission lines that may be observable, but space limitations preclude discussion of other than the 1–0 $S(1)$, 2–1 $S(1)$, and 6–4 $Q(1)$ lines discussed above. Complete H_2 vibration-rotation emission spectra may be obtained via anonymous ftp for the models listed in Table 3. Readers interested in H_2 spectra for other values of χ, n_H, T_0, σ_d, T_f, or b should contact the authors.

7. ROTATIONAL POPULATIONS

The rotational populations within a given vibrational level can be approximated by a thermal distribution,

$$N(v, J)/g_J = a \exp\left[-E(v, J)/kT_r\right], \quad (56)$$

where

$$g_J = (2J + 1) \text{ for even } J(\text{para-H}_2), \quad (57)$$

$$= 3(2J + 1) \text{ for odd } J(\text{ortho-H}_2), \quad (58)$$

and T_r is the apparent "rotational temperature." Because ortho- and para-H_2 may not be fully equilibrated, we allow separate values of a, denoted a_{ortho} and a_{para}, for the ortho- and para-H_2 states, but we fit a single rotational temperature T_r for both ortho- and para-H_2 within a single vibrational level. We define the ratio

$$\gamma \equiv 3a_{\text{ortho}}/a_{\text{para}} \quad (59)$$

to characterize the ortho-para ratio: from our definition of γ, we see that for a thermal distribution we would have $\gamma = 3$, even at low temperatures. Note that γ is *not* the actual ortho/para ratio (i.e., the ratio of the total column densities of the ortho-H_2 and para-H_2), which goes to zero in thermal equilibrium as $T \to 0$.

In Figure 17, we show γ determined by fitting equation (56) to our model calculations; the fit is restricted to the $v = 1$ levels $2 \le J \le 7$. For $n_H \lesssim 10^4$ cm^{-3} and $T_0 \lesssim 700$ K, we find $\gamma \approx 2 \pm 0.2$, essentially independent of χ/n_H.

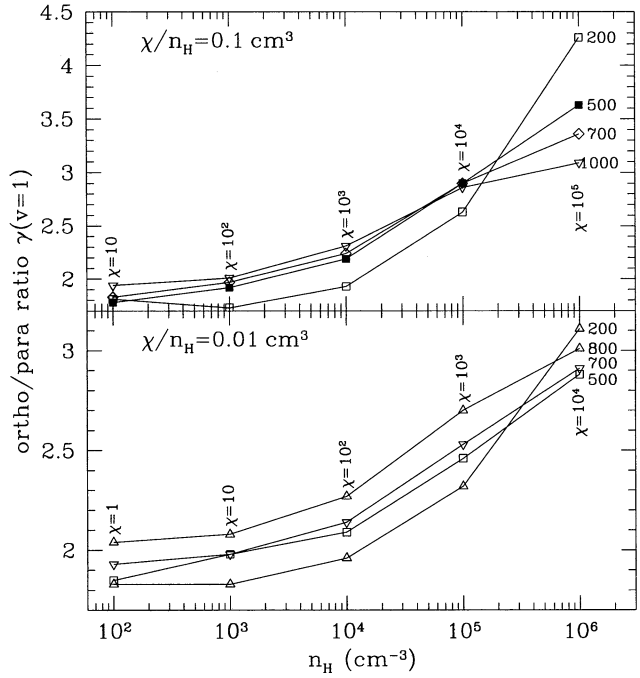

FIG. 17.—Same as Fig. 15, but showing ortho/para ratio parameter γ (see eq. [59]) for H_2 in levels $v = 1, 2 \le J \le 7$. An H^+ fraction $x_H = 10^{-4}$ has been assumed.

As discussed in § 2.4, the H_2 is assumed to be formed on grains with an ortho/para ratio of 2.78, so an appreciably lower value of γ for the $v = 1$ levels reflects ortho → para conversion in the gas. We have assumed $x_H = n(H^+)/n_H = 10^{-4}$ in the present models. In regions with $x_H > 10^{-7}$, the dominant ortho-para conversion process is reactive scattering with H^+, with a rate coefficient $\sim 2 \times 10^{-10}$ cm^3 s^{-1} for $H_2(0, 1) + H^+ \to H_2(0, 0) + H^+$. While this is much slower than photodissociation of H_2 in unshielded regions, note that at the point at which $2n(H_2) = n(H)$, the H_2 photodissociation rate is $\zeta_{\text{diss}} = Rn_H = 6 \times 10^{-17}(T/100\ \text{K})^{0.5}(n_H/\text{cm}^{-3})$ s^{-1}, slow compared to the rate $2 \times 10^{-14}(n_H/\text{cm}^{-3})(x_H/10^{-4})$ s^{-1} for $(0, 1) \to (0, 0)$ conversion by H^+. In regions in which x_H is very small, ortho-para conversion takes place via scattering by H atoms and off grain surfaces.

As n_H is increased above $\sim 10^4$ cm^{-3}, γ increases and approaches ~ 3. Indeed, we see that this non-LTE environment can result in values of $\gamma > 3$: for $\chi = 10^5$, $n_H = 10^6$ cm^{-3}, and $T_0 = 200$ K, our best-fit $\gamma = 4.3$. Note that this occurs under conditions at which UV pumping can compete with spontaneous decay from vibrationally excited levels (see § 3). The observed large value of γ may result from the greater ability of ortho-H_2 to self-shield.

The rotational temperatures $T_r(v = 1)$ and $T_r(v = 2)$ of the $v = 1$ and 2 levels of H_2 are shown in Figures 18 and 19. We see that optical pumping results in rotational temperatures 1000–2000 K. There is a general trend for T_r to increase with increasing χ (e.g., compare lower and upper panels of each figure) because of the increasing importance of optical pumping compared to radiative decay or collisional de-excitation. It is interesting to note that under some conditions, an increase in T_0 leads to a decrease in T_r: for example, at $n_H = 10^4$ cm^{-3} and $\chi = 10^2$, changing T_0 from 500 to 1000 K causes T_r to decrease from 1500 to 1000 K.

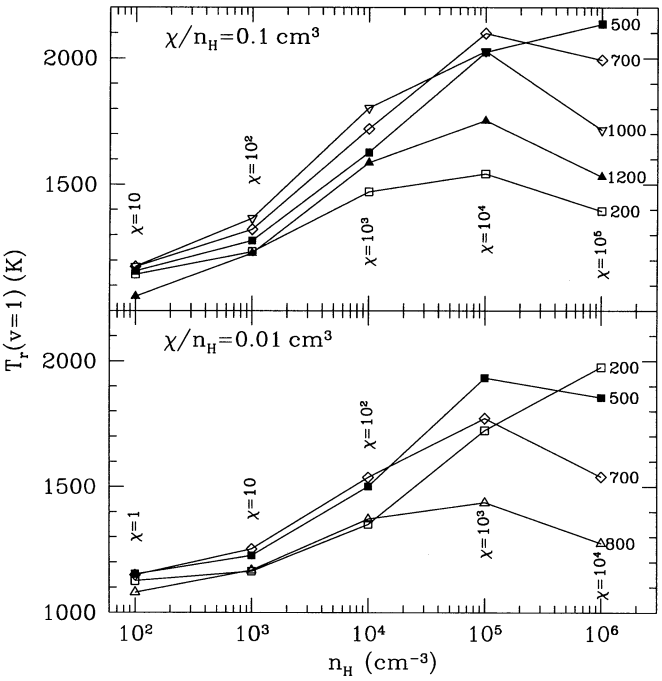

FIG. 18.—Same as Fig. 15, but showing rotational temperature of H_2 in levels $v = 1, 2 \le J \le 7$.

This is due to the large increase in H–H_2 inelastic rate coefficients, which make it possible for collisional processes to compete with radiative pumping, tending to bring T_r toward the gas temperature T.

8. NGC 2023

8.1. *Observations*

The B1.5 V star HD 37903, at an estimated distance $D = 450$ pc, is situated near the edge of the molecular cloud L1630, resulting in the prominent reflection nebula NGC 2023. NGC 2023 displays strong H_2 fluorescent emission, and its spectrum has been studied both in the infrared (Gatley et al. 1987; Hasegawa et al. 1987) and the far-red (Burton et al. 1992). Gatley et al. have mapped the 1–0 $S(1)$ emission, which peaks in an "emission ridge" south-southeast of the star. The brightest spot on the ridge is located about 78″ south, 9″ west of the star (Burton et al. 1989; Field et al. 1994; Brand 1995), corresponding to a transverse distance of $5.3 \times 10^{17}(D/450\ \mathrm{pc})$ cm. Field et al. (1994) have obtained a high-resolution image of NGC 2023 in the 1–0 $S(1)$ line; the brightest spot is 27″ north, 22″ east of the star, with a surface brightness slightly higher than on the southern emission ridge. The C recombination line emission peaks in the vicinity of the southern 1–0 $S(1)$ emission peak (Wyrowski & Walmsley 1996); C recombination line spectroscopy indicates a gas density $n_H \approx 10^5\ \mathrm{cm}^{-3}$ (Pankonin & Walmsley 1976, 1978). Since the only available far-red spectra of NGC 2023 were taken on the southern filament, our modeling objective will be to try to reproduce the observed H_2 spectrum of the southern filament.

A B1.5 V star ($T_{\rm eff} = 22{,}000$ K, $L = 7600\ L_\odot$) radiates $S_{uv} \approx 2.5 \times 10^{47}\ \mathrm{s}^{-1}$ in the 1110–912 Å range (Fitzpatrick 1995, based on Kurucz ATLAS9 model atmospheres); at a distance r from the star,

$$\chi \approx \frac{S_{uv}/4\pi r^2}{1.23 \times 10^7\ \mathrm{cm}^{-2}\ \mathrm{s}^{-1}} = 6400\left(\frac{5 \times 10^{17}\ \mathrm{cm}}{r}\right)^2, \quad (60)$$

neglecting dust extinction. Harvey, Thronson, & Gatley (1980) conclude that most of the infrared-emitting dust is more than 0.1 pc from HD 37903. We therefore assume that there is only modest absorption by dust between the star and the H_2 emission ridge and seek to reproduce the observed H_2 line spectra by a model of a plane-parallel stationary photodissociation region illuminated by radiation with $\chi \approx 5000$. The idealized geometry is shown in Figure 20.

The computed surface brightnesses will of course depend on the adopted value of the angle θ. Since the highest fluorescent surface brightness will presumably be in a region in which there is significant limb-brightening, we need to estimate the likely magnitude of this effect. A shell with inner and outer radii r_i and $r_i + \Delta r$, containing material with emissivity j, would have a peak surface brightness (in the absence of internal extinction) $j(8r_i\Delta r)^{1/2}(1 + \Delta r/2r_i)^{1/2}$. Viewed face-on, a portion of the shell would have surface brightness $j\Delta r_i$, so that limb-brightening enhances the surface brightness over that of a plane-parallel slab viewed normally by a factor $B = (8r_i/\Delta r)^{1/2}(1 + \Delta r/2r_i)^{1/2}$. For $n_H \approx 10^5 n_5\ \mathrm{cm}^{-3}$ and UV extinction cross section $\sigma_{1000} \approx 6 \times 10^{-22}\ \mathrm{cm}^2$, we would estimate the thickness of the fluorescing region to be $\Delta r \approx (n_H \sigma_{1000})^{-1} \approx 1.7 \times 10^{16} n_5^{-1}$ cm. Taking $r_i \approx 5 \times 10^{17}$ cm, we then estimate a peak geometric limb-brightening factor $B \approx 15 n_5^{1/2}$. We regard this as an upper limit to the value of $(\cos\theta)^{-1}$. If the local radius of curvature of the PDR at the surface of a "filament" is smaller than the distance to the star, the peak limb-brightening factor will be smaller than this upper limit.

A convenient way to compare with observations is to plot $N_{\rm obs}(v, J)/g_J$ versus $E(v, J)$, where $E(v, J)$ is the energy and g_J is the degeneracy of the (v, J) level. The "observed"

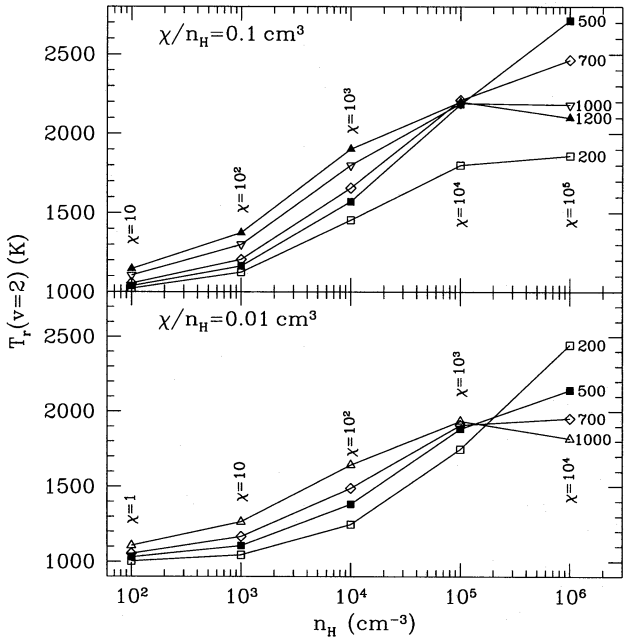

FIG. 19.—Same as Fig. 18, but for levels $v = 2, 2 \le J \le 7$

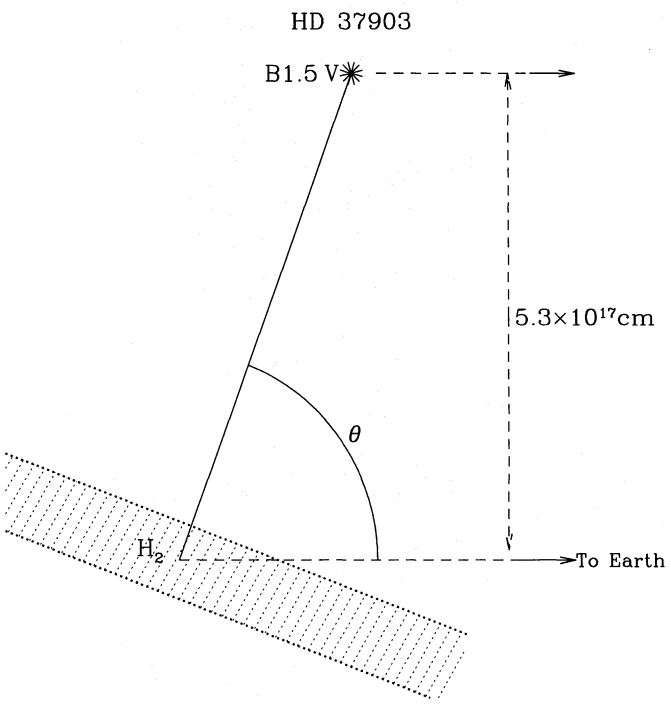

FIG. 20.—Slab geometry assumed for the H_2 "emission ridge" observed for NGC 2023.

$N_{obs}(v, J)$ values are obtained from equation (55).[7] We characterize the extinction by A_K and have used the CCM extinction curve for $R_V = 5.5$ to estimate A_λ/A_K. Burton (1993) has estimated the K-band extinction to be $A_K = 0.3$ mag; we assume a slightly smaller extinction $A_K = 0.2$ mag, which corresponds to extinction by dust with $E(B-V) \approx 1.37A_K = 0.27$ mag and $A_V = 1.5$ mag. The extinction at 0.9 and 0.7 μm is estimated to be $A_{0.9} = 4.2A_K = 0.84$ mag and $A_{0.7} = 6.0A_K = 1.2$ mag.

There are three levels ($v = 3$, $J = 3$, 4, 5) for which emission has been reported by both Hasegawa et al. (1987, hereafter H87) and Burton et al. (1992, hereafter B92). Unfortunately, after correcting for differential extinction, the column densities $N_{obs}(v, J)$ derived from the B92 far-red spectrum are a factor of ~10–20 larger than those derived from the K-band observations of H87! For example, the 3–2 $S(3)$ flux observed by H87, corrected for reddening by $A_K = 0.2$ mag, corresponds to $N_{obs}(3, 5) = 2.5 \times 10^{14}$ cm^{-2}. However, the 3–0 $S(3)$ flux reported by B92, corrected for reddening by $A_{0.7962\,\mu m} = 5.08A_K = 1.02$ mag, corresponds to $N_{obs}(3, 5) = 3.4 \times 10^{15}$ cm^{-2}—a factor of 13 larger than inferred from the K-band spectra! Discrepancies of 21 and 15 are found for the (3, 3) and (3, 4) levels, although for these levels the reported uncertainties in the fluxes are greater. We will assume an overall discrepancy of 15 between the H87 and B92 column densities. The fluorescent emission is strongly peaked on the "emission ridge" (Burton et al. 1989; Brand 1995), and the differences between H87 and B92 are in large part due to the fact that H87 used a 19".6 diameter beam while B92 used a 27" × 1" aperture aligned along the emission ridge. We will assume that the H87 surface brightnesses need to be multiplied by a factor $\beta_{H87} = 6$ to correct for beam dilution, but that the B92 fluxes should be multiplied by a factor $\beta_{B92} = \beta_{H87}/15 = 0.40$ to correct for an apparent calibration error.[8]

8.2. *Models for the NGC 2023 PDR*

We consider two stationary PDR models for the NGC 2023 emission ridge. Both have $\chi = 5000$, $n_H = 1 \times 10^5$ cm^{-3}, and a viewing angle $\theta = \cos^{-1} 0.2 \approx 78°$. We assume the temperature profile in the PDR to be given by equation (41) and consider two values of T_0: model A has $T_0 = 500$ K, and model B has $T_0 = 900$ K. Both models have $\chi/n_H = 0.05$ cm^3; $\phi_0 = 0.12$ for model A and 0.086 for model B. From Figure 11, for both models we expect most of the vibrationally excited H_2 to be within the first $N_H = 1.5 \times 10^{21}$ cm^{-2}, or 1.5×10^{16} cm, corresponding to ~2" at the distance of NGC 2023. This is consistent with the observed narrowness of the "emission ridge."

The pumping efficiency $\epsilon_{pump} = 0.69$ for model A and 0.74 for model B, somewhat larger than the estimates ~0.45 from equation (48); the enhancement of ϵ_{pump} results from the substantial populations of H_2 in excited rovibrational levels, so that UV absorption by H_2 is spread over more lines, including many with $\lambda > 1110$ Å. The models succeed in reproducing most of the observed intensities to within a factor ~2. As we shall see, model B appears to be in fairly good agreement with the published observations for NGC 2023.

8.3. *1–0 S(1)/2–1 S(1) Ratio*

Hasegawa et al. find 1–0 $S(1)$/2–1 $S(1) = 3.7 \pm 0.6$; from Figure 2 of Burton (1993), we infer a value of 3.0 for this ratio. These are both well above the calculated value for our model A, which has 1–0 $S(1)$/2–1 $S(1) = 2.20$, a value typical of UV pumping. Model B, with a higher gas temperature, has 1–0 $S(1)$/2–1 $S(1) = 2.91$; this is in part due to collisional excitation of the $v = 1$ level and in part due to preferential collisional de-excitation of UV-pumped $v = 2$, as discussed in § 7. Varying T_0 between 800 and 1000 K allows us to obtain 1–0 $S(1)$/2–1 $S(1)$ ratios between 2.54 and 3.90. We consider model B to be in good agreement with the observed 1–0 $S(1)$/2–1 $S(1)$ ratio.

8.4. *Rotational Temperatures and Ortho-Para Ratio*

In Figures 21 and 22, one sees that there is fairly good overall agreement between predicted and observed line intensities. Figures 21 and 22 show the least-squares fit to the rotational temperature T_r characterizing rotational levels $2 \le J \le 7$ for each vibrational level. H87 obtained a rotational temperature $T_r = 900$ K for the $v = 1$, $J = 2$–4 levels. If we restrict our least-squares fit to these three levels, we obtain $T_r = 1217$ K and $\gamma = 2.36$ for model A and $T_r =$

[7] Note that the column densities $N(v, J)$ (uncorrected for extinction) reported by Burton et al. (1992) are not consistent with their reported intensities because of a multiplicative error (Burton 1995); the Burton et al. column densities must be reduced by a factor 0.36 to bring them into agreement with the reported intensities.

[8] Note that with the H87 intensities increased by a factor of 6, the B92 intensities would not require correction if there were no differential extinction between the K-band and the far-red. This possibility does not seem likely, however, as even the dust within the PDR should contribute extinction with an effective $A_K \approx 0.2$.

1160 K, $\gamma = 2.46$ for model B, in reasonable agreement with H87.

H87 found $T_r \approx 1500 \pm 200$ K for the $v = 2$, $J = 2$–5 levels. For these four levels, our least-squares fit gives $T_r = 1587$ K for model A and $T_r = 1650$ K for model B.

For the higher vibrational levels, we also do a fairly good job of reproducing the relative populations of the different J levels, as can be seen for the $v = 3$, 4, 7, and 8 levels in Figures 21 and 22.

Our ortho-para ratios are somewhat above the observed values. Burton (1993) finds that the observed line intensities are consistent with $\gamma = 2.1 \pm 0.2$ for all levels, whereas we find (for model B) $\gamma = 2.46$ for $v = 1$ ($J = 2$–4) and $\gamma = 2.46$ for $v = 2$ ($J = 2$–5).

8.5. *Spectra*

We have taken the predicted emission spectra for the above models and convolved them with a Gaussian with $\lambda/\mathrm{FWHM}_\lambda = 2000$ ($\mathrm{FWHM}_v = 150$ km s^{-1}). The spectra include the effects of extinction within the emitting slab, but no additional foreground extinction is allowed for. In Figures 23 and 24, we show the predicted emission spectra for models A and B. The far-red lines derive from transitions from high-v states, for which the collisional de-excitation rate coefficients are much larger than for the low-v states. Note that the far-red emission is relatively stronger in model A than in model B—this is because there is more collisional de-excitation in model B because of the higher temperature. A list of all the H_2 lines with intensities exceeding 0.1% of 1–0 $S(1)$ (1280 and 1174 lines for models A and B, respectively) is available via anonymous ftp (see Table 3).

8.6. *Discussion*

Black & van Dishoeck (1987) have previously put forward models for the fluorescent emission from NGC 2023. Their models had $I_{\mathrm{UV}} = 300$, which (see Table 1) corresponds to $\chi \approx 670$—a factor of 7.5 weaker than the $\chi = 5000$ favored here. The reported 1–0 $S(1)$ *face-on* surface brightness for their "reference model A" is 3.5×10^{-5} ergs cm^{-2} s^{-1} sr^{-1}, corresponding to an "efficiency" $\epsilon_{1-0\,S(1)} = 0.058$. We have computed a model

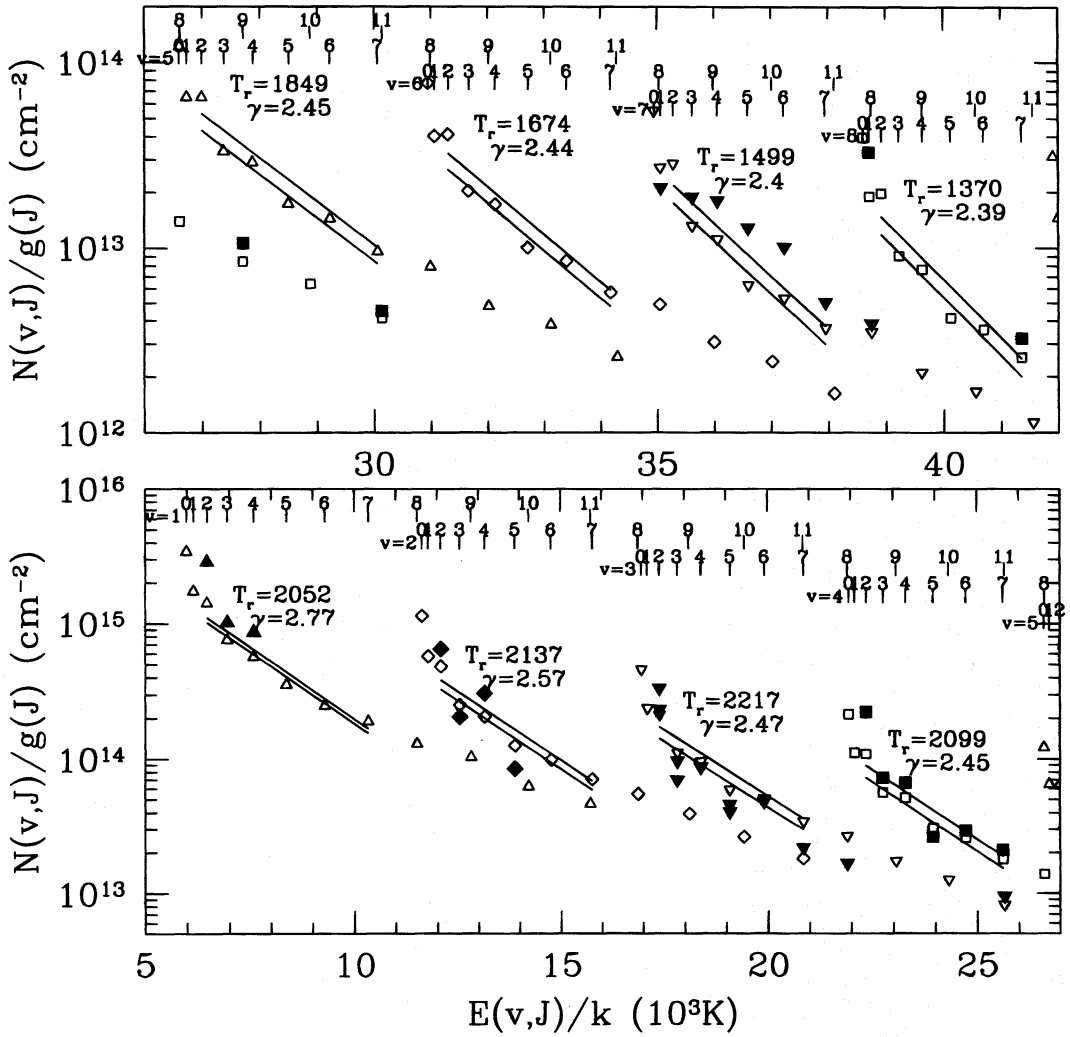

FIG. 21.—Column densities $N(v, J)$ divided by the level degeneracy $g(J)$ for the NGC 2023 emission ridge. Filled symbols are derived from observations of Hasegawa et al. (1987) and Burton et al. (1992), corrected for extinction with $A_K = 0.2$ mag. Surface brightnesses reported by Hasegawa et al. (1987) have been multiplied by 6 to allow for beam dilution (see text); surface brightnesses of Burton et al. have been reduced by a factor 0.4 for consistency (see text). Open symbols are for a plane-parallel slab model with $\chi = 5000$, $n_{\mathrm{H}} = 10^5$ cm^{-3}, and $T_0 = 500$ K, viewed at an angle with cos $\theta = 0.2$. Solid lines are least-squares LTE fits to the $2 \le J \le 7$ populations in each vibrational level. For each vibrational level, the best-fit values of the rotational temperature T_r and ortho/para ratio parameter γ are indicated.

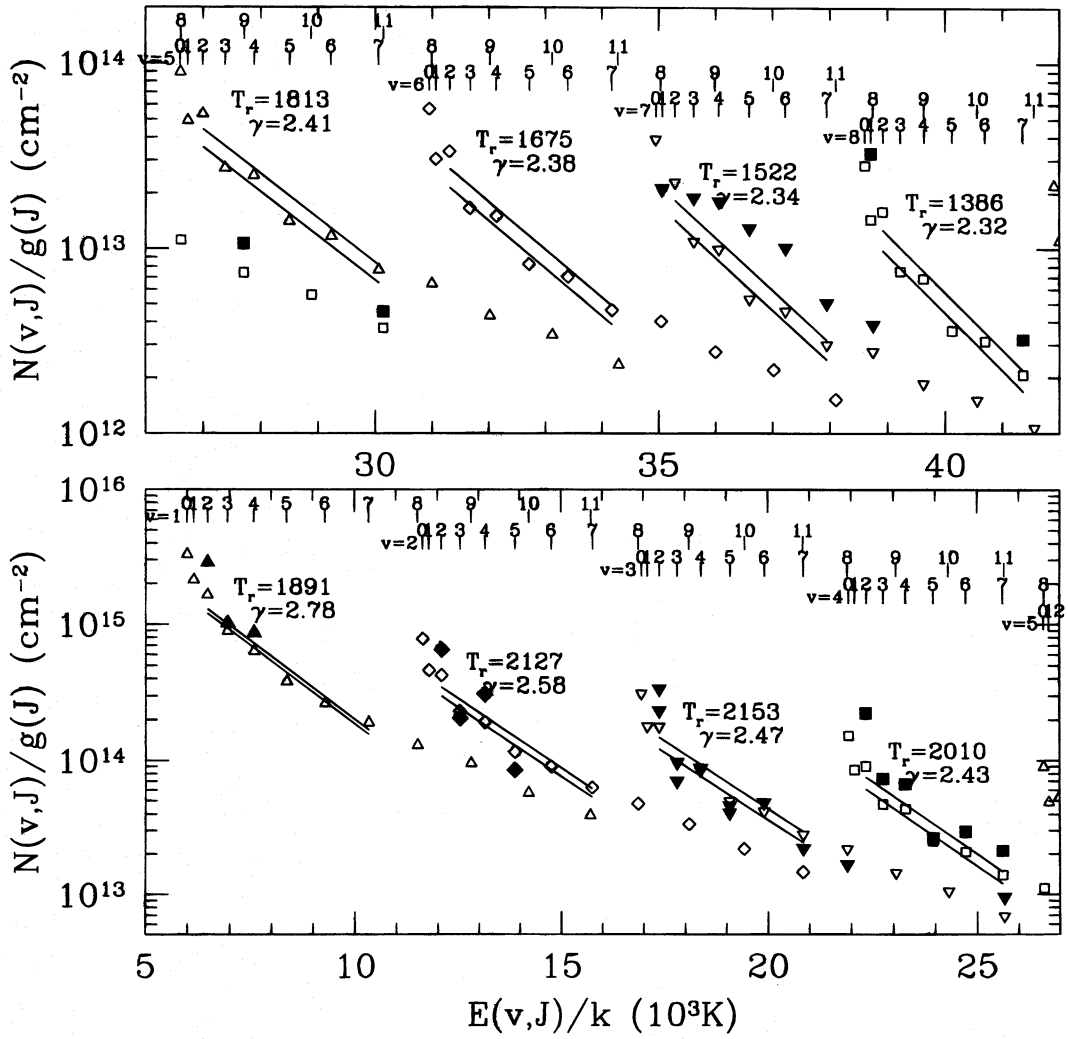

FIG. 22.—Same as Fig. 21, but for model B, with $\chi = 5000$, $n_H = 10^5$ cm^{-3}, $T_0 = 900$ K, and cos $\theta = 0.2$

with $\chi = 670$, $n_H = 10^4$ cm^{-3}, $T = 80$ K, and the same grain properties (extinction and H_2 formation rate) as assumed by Black & van Dishoeck for their reference model A; we obtain an efficiency $\epsilon_{1-0\,S(1)} = 0.021$, a factor of 2.7 smaller than obtained by Black & van Dishoeck. Part of the discrepancy is attributable to the fact that Black & van Dishoeck did not allow for the effects of line overlap; if we modify our model to neglect line overlap (by taking $W_{max} \rightarrow \infty$ in eq. [30]), the 1–0 $S(1)$ surface brightness increases by a factor of 1.5. The remaining discrepancy, amounting to a factor of 2.7/1.5 = 1.8, may be due in part to the fact that we use improved (larger) dissociation probabilities for the C^+ levels, although this seems unlikely to explain the factor of 1.8.

The Black & van Dishoeck models were developed with the aim of reproducing the surface brightnesses reported by H87. As discussed in § 8.1, we now believe the peak 1–0 $S(1)$ surface brightness to be a factor ~6 higher than reported by H87, so the published Black & van Dishoeck models are not applicable to the bright bar in NGC 2023.

Our modeling efforts lead us to conclude that if the dissociation front is approximately stationary, then the fluorescing H_2 in the NGC 2023 emission ridge must have $n_H \approx 10^5$ cm^{-3} and appreciable limb-brightening (such as cos $\theta = 0.2$, as in our models A and B) in order to reproduce the observed high surface brightness. Lowering n_H (increasing χ/n_H) would lead to somewhat lowered fluorescent efficiency and, by reducing the importance of collisional effects, would make it difficult to reproduce the observed 1–0 $S(1)$/2–1 $S(1)$ line ratio, which requires a combination of collisional de-excitation from $v = 2$ and collisional excitation from $v = 0$ to 1. On the other hand, increasing n_H would result in increased collisional de-excitation of vibrationally excited levels, which would make it difficult to reproduce the observed high surface brightnesses. It is reassuring that our density estimate $n_H \approx 10^5$ cm^{-3} is in agreement with that deduced by Pankonin & Walmsley (1976, 1978) from C recombination lines, which should originate from the same gas. Jansen, van Dishoeck, & Black (1994) have used the observed HCO^+ 3–2/4–3 line ratio to infer $n_H \approx 5 \times 10^4$ cm^{-3} in this region. Fuente, Martín-Pintado, & Gaume (1995) have argued for $n_H \approx 10^6$ cm^{-3} near the photodissociation front based on observations of CN, SO, and HCN rotational lines.

Our best model (B) does not fully reproduce the observed line surface brightnesses (see Fig. 22). There are a number of possible explanations:

1. The emission bar may include a range of densities, whereas in our modeling we seek to explain the observations with a single density.

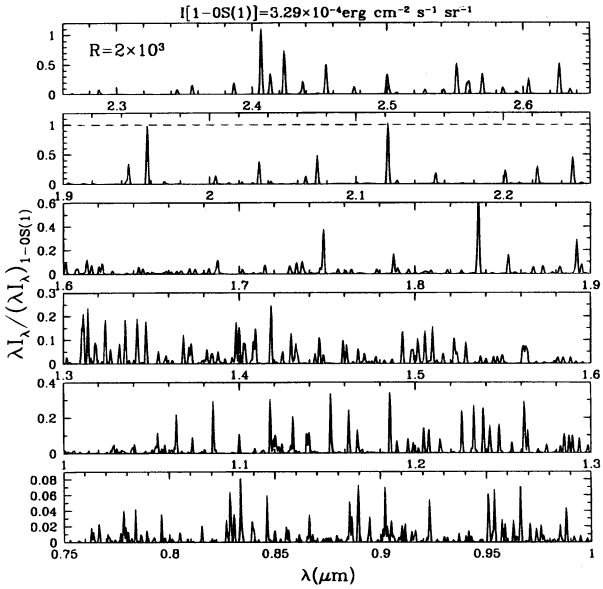

FIG. 23.—Emission spectrum for NGC 2023 model A ($\chi = 5000$, $n_H = 10^5$ cm^{-3}, $T_0 = 500$ K) viewed from a direction with $\cos\theta = 0.2$. The spectrum is convolved with a Gaussian response function with $R = \lambda/\mathrm{FWHM}_\lambda = 2 \times 10^3$. Extinction by dust within the PDR has been included, but no external dust has been allowed for.

2. The actual temperature profile may be rather different from that assumed here.

3. Line overlap effects will suppress particular photoexcitation transitions, whereas in our treatment we share this suppression among all of the transitions with $1110 < \lambda < 912$ Å.

4. As discussed in § 2.2, the actual branching ratios following photoexcitation in the damping wings may differ from our adopted branching ratios, thereby altering relative line strengths.

5. Errors in our adopted collisional rate coefficients may be important, since the vibrationally excited states may be collisionally de-excited at the densities $n_H \approx 10^5$ cm^{-3} assumed here.

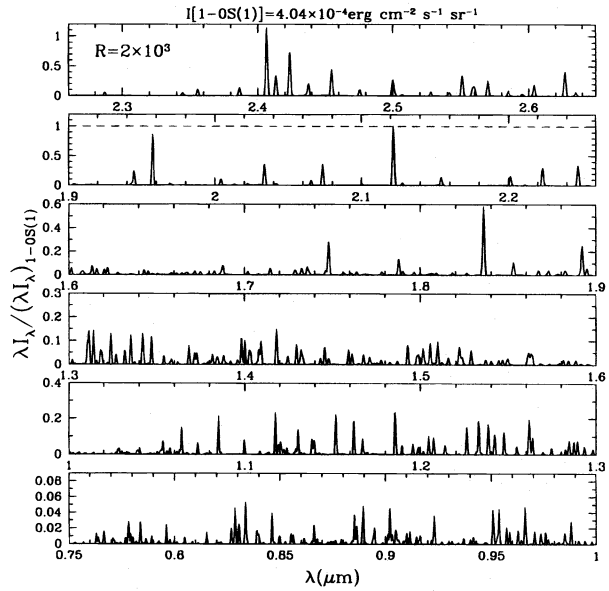

FIG. 24.—Same as Fig. 23, but for model B with $T_0 = 900$ K

6. The dissociation front in NGC 2023 may be propagating rapidly enough that the stationary approximation made here leads to errors.

NGC 2023 shows structure on $\sim 1''$ scales (Field et al. 1994). We need calibrated H_2 spectral line images of NGC 2023 in a number of H_2 fluorescence lines to test the accuracy of our models.

9. SUMMARY

The principal results of this paper are as follows:

1. An approximate treatment of self-shielding (eq. [30]) is developed that treats line overlap in a statistical fashion. This treatment allows individual lines to be treated using the single-line equivalent width approximation but allows statistically for overall suppression of the continuum due to line overlap. Comparison with exact calculation shows this approximation to be accurate.

2. Two simple approximations are provided for the self-shielding function for H_2. The first, a simple power law (eq. [36]), provides a fairly good fit to self-shielding over the range $10^{15} < N_2 < 10^{21}$ cm^{-2}. The second (eq. [37]) is an analytic function that provides a very good approximation to the self-shielding including the effects of line overlap. These functions are recommended for use in future studies of photodissociation regions.

3. The effects of line overlap become important for column densities $N(H_2) \gtrsim 10^{20}$ cm^{-2}, suppressing the UV pumping rate by a factor of 2 at $N(H_2) \approx 3 \times 10^{20}$ cm^{-2} (see Fig. 6).

4. For dense cloud dust properties, the effects of line overlap become important while the dust is still optically thin for $\chi/n_H \lesssim 0.05$ (see Fig. 10).

5. The dust optical depth τ_{pdr} at the point at which $2n(H_2) = n(H)$ is primarily a function of a single parameter $\phi_0 \propto (\chi/n_H R)\sigma_{1000}^{3/4}$, defined in equation (44). The approximation (46) provides a good estimate for τ_{pdr}.

6. The "efficiency" of UV pumping of H_2 in the photodissociation front, ϵ_{pump}, is also a function of the single parameter ϕ_0 and is approximately given by equation (48).

7. For $n_H \lesssim 10^5$ cm^{-3}, the efficiency $\epsilon_{1-0\,S(1)}$ for 1–0 $S(1)$ emission is given as a function of ϕ_0 and χ by equation (50).

8. The emission from PDRs is quite insensitive to the color temperature of the illuminating radiation for color temperatures $T_{color} \gtrsim 10^4$ K or stars with spectral type A0 or earlier.

9. The emission spectrum from low J levels [e.g., 1–0 $S(1)$, or 3–2 $S(1)$] is insensitive to the distribution function $\delta(v, J)$ of newly formed H_2, but the emission from higher J levels [e.g., 1–0 $S(9)$] is increased (by a factor ~ 2) when the newly formed H_2 is rotationally "hot."

10. Observable properties of photodissociation fronts—including the 1–0 $S(1)$/2–1 $S(1)$ line ratio (Fig. 15), the 2–1 $S(1)$/6–4 $Q(1)$ line ratio (Fig. 16), the ortho/para ratio (Fig. 17), and the rotational temperatures (Figs. 18 and 19)—are computed for various values of χ, n_H and temperature. Complete H_2 vibration-rotation spectra are available via anonymous ftp.

11. The reflection nebula NGC 2023 is considered. We correct the H87 intensities for assumed beam dilution and adjust the B92 intensities for consistency. The (adjusted) observations are approximately reproduced by a model

with $n_H = 10^5$ cm^{-3} and $\chi = 5000$, with $T_0 \approx 900$ K. The agreement is not perfect; possible explanations for the discrepancies are discussed.

We are especially grateful to P. W. J. L. Brand and M. Walmsley for communicating recent observations of NGC 2023 in advance of publication, to E. L. Fitzpatrick for computing S_{uv} for B stars, to R. H. Lupton for making available the SM plotting package, to P. G. Martin for making available H-H_2 rate coefficients in advance of publication, and to E. Roueff for kindly providing us with molecular data for H_2 in computer-readable form. We wish also to thank M. G. Burton, E. van Dishoeck, D. Neufeld, M. Walmsley, D. T. Jaffe, and E. Roueff for helpful comments and discussions.

This research was supported in part by NSF grant AST 93-19283, and by the Deutsche Forschungsgemeinschaft.

REFERENCES

Abgrall, H., Le Bourlot, J., Pineau des Forêts, G., Roueff, E., Flower, D. R., & Heck, L. 1992, A&A, 253, 525
Abgrall, H., & Roueff, E. 1989, A&AS, 79, 313
Abgrall, H., Roueff, E., Launay, F., Roncin, J.-Y., & Subtil, J.-L. 1993a, A&AS, 101, 273
———. 1993b, A&AS, 101, 323
Bakes, E. L. O., & Tielens, A. G. G. M. 1994, ApJ, 427, 822.
Bertoldi, F., & Draine, B. T. 1996, ApJ, 458, 222
Black, J. H., & Dalgarno, A. 1976, ApJ, 203, 132
———. 1977, ApJS, 34, 405
Black, J. H., Porter, A., & Dalgarno, A. 1981, ApJ, 249, 138
Black, J. H., & van Dishoeck, E. F. 1987, ApJ, 322, 412
Bohlin, R. C., Savage, B. D., & Drake, J. F. 1978, ApJ, 224, 132
Brand, P. W. J. L. 1995, private communication
Burton, M.G. 1993, Proc. Astron. Soc. Australia, 10, 322
———. 1995, private communication
Burton, M. G., Bulmer, M., Moorhouse, A., Geballe, T. R., & Brand, P. W. J. L. 1992, MNRAS, 257, 1P (B92)
Burton, M. G., Hollenbach, D. J., & Tielens, A. G. G. M. 1990, ApJ, 365, 620
Burton, M. G., Moorhouse, A., Brand, P. W. J. L., Roche, P. F., & Geballe, T. R. 1989, in Interstellar Dust: Contributed Papers (NASA Conf. Publ. 3036), ed. A. G. G. M. Tielens & L. J. Allamandola (Washington : NASA), 87
Cardelli, J. A., Clayton, G. C., & Mathis, J. S. 1989, ApJ, 345, 245 (CCM)
de Jong, T., Dalgarno, A., & Boland, W. 1980, A&A, 91, 68
Draine, B. T. 1978, ApJS, 36, 595
Draine, B. T., & Bertoldi, F. 1996, in preparation
Draine, B. T., & Lee, H. M. 1984, ApJ, 285, 89
Federman, S. R., Glassgold, A. E., & Kwan, J. 1979, ApJ, 227, 466
Field, D., Gerin, M., Leach, S., Lemaire, J. L., Pineau des Forêts, G., Rostas, F., Rouan, D., & Simons, D. 1994, A&A, 286, 909
Field, G. B., Somerville, W. B., & Dressler, K. 1966, ARA&A, 4, 226
Fitzpatrick, E. L. 1995, private communication
Fuente, A., Martín-Pintado, J., & Gaume, R. 1995, ApJ, 442, L33
Gatley, I., et al. 1987, ApJ, 318, L73
Goldschmidt, O., & Sternberg, A. 1995, ApJ, 439, 256
Gould, R. J., & Harwit, M. 1963, ApJ, 137, 694
Green, L. C., Rush, P. P., & Chandler, C. D. 1957, ApJS, 3, 37
Habing, H. J. 1968, Bull. Astron. Inst. Netherlands, 19, 421
Harvey, P. M., Thronson, H. A., & Gatley, I. 1980, ApJ, 235, 894
Hasegawa, T., Gatley, I., Garden, R. P., Brand, P. W. J. L., Ohishi, M., Hayashi, M., & Kaifu, N. 1987, ApJ, 318, L77 (H87)
Heck, E. L., Flower, D. R., Le Bourlot, J., Pineau des Forêts, G., & Roueff, E. 1992, MNRAS, 258, 377
Hill, J. K., & Hollenbach, D. J. 1978, ApJ, 225, 390
Hollenbach, D. J., & Natta, A. 1995, ApJ, 455, 133
Jansen, D. J., van Dishoeck, E. F., & Black, J. H. 1994, A&A, 282, 605
Jura, M. 1975, ApJ, 197, 575
Le Bourlot, J., Pineau des Forêts, G., Roueff, E., & Flower, D. R. 1992, A&A, 267, 233
Lepp, S., Buch, V., & Dalgarno, A. 1995, ApJS, 98, 345
Luhman, M. L., & Jaffe, D. T. 1996, ApJ,463, 1
Mandy, M. E., & Martin, P. G. 1993, ApJS, 86, 199
———. 1996, J. Chem. Phys., in preparation
Martin, P. G., & Mandy, M. E. 1995, ApJ, 455, L89
Mathis, J. S. 1990, ARA&A, 28, 37
Mathis, J. S., Mezger, P. G., & Panagia, N. 1983, A&A, 128, 212
Mathis, J. S., Rumpl, W., & Nordsieck, K. H. 1977, ApJ, 217, 425
O'Donnell, J. E. 1994, ApJ, 422, 153
Pankonin, V., & Walmsley, C. M. 1976, A&A, 48, 341
———. 1978, A&A, 67, 129
Press, W. H., Flannery, B. P., Teukolsky, S. A., & Vetterling, W. T. 1992, Numerical Recipes (2d ed.; Cambridge: Cambridge Univ. Press)
Roberge, W. G. 1981, Ph.D. thesis, Harvard Univ.
Roberge, W. G., Dalgarno, A., & Flannery, B. P. 1981, ApJ, 243, 817
Rodgers, C. D., & Williams, A. P. 1974, J. Quant. Spectrosc. Rad. Transf., 14, 319
Roueff, E. 1992, private communication
Shull, J. M. 1978, ApJ, 219, 877
Stecher, T. P., & Williams, D. A. 1967, ApJ, 149, L29
Stephens, T. L., & Dalgarno, A. 1972, J. Quant. Spectrosc. Radiat. Transfer, 12, 569
Sternberg, A. 1986, Ph.D. thesis, Columbia Univ.
———. 1988, ApJ, 332, 400
Sternberg, A., & Dalgarno, A. 1989, ApJ, 338, 197
Tielens, A. G. G. M., & Allamandola, L. J. 1987, in Interstellar Processes, ed. D. J. Hollenbach & H. A. Thronson (Dordrecht: Kluwer), 397
Tielens, A. G. G. M., & Hollenbach, D. J. 1985a, ApJ, 291, 722
———. 1985b, ApJ, 291, 747
van Dishoeck, E. F., & Black, J. H. 1986, ApJS, 62, 109
Witt, A. N., Petersohn, J. K., Holberg, J. B., Murthy, J., Dring, A., & Henry, R. C. 1993, ApJ, 410, 714
Wyrowski, F., & Walmsley, M. 1996, in preparation